Accepted paper

J. Cardoso, J. Gwenolé, D.Nd. Faye, A.M. Siladie, B. Daudin, E. Alves, K. Lorenz, T. Monteiro, M.R. Correia, N. Ben Sedrine.

Eu3+ optical activation engineering in Al Ga1-N nanowires for red solid-state nano-emitters. Applied Materials Today, Elsevier, 2021, 22, pp.100893. 10.1016/j.apmt.2020.100893.

Eu^{3+} optical activation engineering in $Al_xGa_{1-x}N$ nanowires for red solid-state nano-emitters

J. Cardoso,[*,†] *G. Jacopin,*[⊥] *D. Nd. Faye,*[‡,□] *A. M. Siladie,*[‖] *B. Daudin,*[‖] *E. Alves,*[♯] *K. Lorenz,*[‡,□] *T. Monteiro,*[†] *M. R. Correia*[†] *and N. Ben Sedrine*[*,†]

[†]Departamento de Física e I3N, Universidade de Aveiro, Campus Universitário de Santiago, 3810-193 Aveiro, Portugal
[⊥]Univ. Grenoble Alpes, CNRS, Grenoble INP, Institut Néel, 38000 Grenoble, France
[‡]IPFN, Instituto Superior Técnico, Campus Tecnológico e Nuclear, Estrada Nacional 10, P-2695-066 Bobadela LRS, Portugal
[‖]Univ. Grenoble Alpes, CEA/CNRS Group, "Nanophysique et Semiconducteurs", F-38000 Grenoble, France
[□]Instituto de Engenharia de Sistemas de Computadores – Microsystems and Nanotechnology (INESC-MN), Rua Alves Redol, 1000-029 Lisboa, Portugal

*Correspondence to jose.cardoso@ua.pt, and nbensedrine@ua.pt

ABSTRACT

In this work, Eu^{3+}-implanted and annealed $Al_xGa_{1-x}N$ ($0 \leq x \leq 1$) nanowires (NWs) grown on GaN NW template on Si (111) substrates by plasma-assisted molecular beam epitaxy are studied by μ-Raman, cathodoluminescence (CL), nano-CL, and temperature-dependent steady-state photoluminescence. The preferential location of the Eu^{3+}-implanted ions is found to be at the $Al_xGa_{1-x}N$ top-section. The recovery of the as-grown crystalline properties is achieved after rapid thermal annealing (RTA). After RTA, the red emission of the Eu^{3+} ions is attained for all the samples with below and above bandgap excitation. The $^5D_0 \rightarrow {}^7F_2$ transition is the most intense one, experiencing a redshift with increasing AlN nominal content (x) from GaN to AlN NWs. Moreover, AlN nominal content and annealing temperature alters its spectral shape suggesting the presence of at least two distinct optically active Eu^{3+} centers (Eu1 and Eu2). Thermal quenching of the Eu^{3+} ion luminescence intensity, I, is found for all the samples from 14 K to 300 K, being the emission of Eu^{3+}-implanted AlN NWs after RTA at 1200 °C the most stable ($I_{300\,K}/I_{14\,K}$ ~80%). The GaN/AlN interface in this sample is also found to have a key role in the Eu^{3+} optical activation.

KEYWORDS

$Al_xGa_{1-x}N$, nanowires, europium, luminescence, red-emitters

1. INTRODUCTION

The nanowire (NW) configuration in semiconductor systems such as oxides, nitrides, and arsenides is highly promising for the next generation nanoscale photonic, optoelectronic and photovoltaic devices thanks to the characteristic large area to volume ratio [1–3]. In particular, for light-emitting devices, it was demonstrated that group III-nitride (III-N) NWs can achieve higher light extraction compared to their 2D counterparts [4,5]. Furthermore, the efficient strain relaxation during NW growth allows the use of highly lattice-mismatched substrates (*e.g.*, silicon) with a reduced density of extended defects compared to thin-film epitaxy, facilitating their compatibility with current microtechnology. III-N nanostructures, with a direct and tunable bandgap energy from 6.2 eV (AlN) to 0.7 eV (InN), have shown unique properties suitable for light-emitting diodes (LEDs), micro-LED technology, and solid-state lasers operating in a wide range of the electromagnetic spectrum [6–12].

The implementation of micro-LED emissive displays requires a monolithic integration of independently controlled red-green-blue (RGB) LEDs to attain high emission efficiency and thermal stability [13]. Blue and green LEDs are obtained by $In_xGa_{1-x}N$ bandgap/nanostructure engineering. However, when further increasing InN content, necessary to achieve red emission, the efficiency is greatly reduced due to lower crystalline quality and increased piezoelectric/spontaneous polarization [14,15]. Thus, a practical and viable strategy is needed to improve the efficiency of III-N red-emitters for monolithic integration of RGB LEDs.

The incorporation of the rare-earth (RE) trivalent europium ions (Eu^{3+}) into III-N layers [16–23] and nanostructures [24–32] was proved as an excellent strategy to obtain red emission characterized by the sharp and stable Eu^{3+} intra-$4f^6$ transitions. This approach was successfully implemented for *in situ* Eu^{3+}-doped GaN-based emitting devices [31,33–38], with Eu^{3+}-related luminescence external quantum efficiency (EQE) values reaching ~29% at room temperature (RT) and ~48% at 77 K [39]. In order to sustain the EQE value up to RT, it is important to overcome the RE thermal quenching. Indeed, as a possible solution, it was proposed that wider bandgap semiconductors show weaker RE thermal quenching [40,41], therefore paving the way to further explore the incorporation of RE in $Al_xGa_{1-x}N$ and AlN hosts.

As an alternative to *in situ* RE incorporation, *ex-situ* ion implantation constitutes a suitable method to obtain a controlled doping profile with concentration even beyond solubility limits [18,25,26,32,42–47]. This technique requires post-implantation thermal annealing to recover the implantation-induced damage and to optically activate the RE ions. Nevertheless, previous reports indicate that the ion implantation-induced damage decreases with increasing AlN content in $Al_xGa_{1-x}N$ layers [48–50], which is an additional argument to explore such materials. To the best of our knowledge, studies on ternary $Al_xGa_{1-x}N:Eu^{3+}$ over the entire range of AlN content were only performed in layers and revealed a reduced thermal quenching with enhanced Eu^{3+} luminescence efficiency for high AlN content hosts [18,51,52]. Besides, Eu^{3+}-implantation in III-N NWs can play a key role for improving Eu^{3+} luminescence efficiency [26–28]: on the one hand, NWs are expected to be less affected by residual implantation-induced damage compared to 2D structures [25]; and on the other hand, Eu^{3+}-implantation occurs not only on the upper surface (*c*-plane) but also on side facets. Although this increases the complexity of implantation damage build-up since crystallographic surface planes can lead to distinct damage in GaN during implantation [53,54], it provides an additional parameter to control the distribution of Eu^{3+} and defects within the NW via the implantation geometry [25]. Furthermore, it was shown that the

formation of extended defects during ion implantation is reduced for NWs as compared with thin films [25].

Therefore, exploring Eu^{3+}-implantation of $Al_xGa_{1-x}N$ NWs turns out to be a very promising strategy for efficient red light-emitting devices with expected lower implantation damage, lower thermal quenching, higher efficiency, and higher light extraction. In the present work, the Eu^{3+} luminescence, achieved after RTA, is studied with emphasis on the most intense $^5D_0 \rightarrow {}^7F_2$ transition. Both excitations, above and below the hosts' bandgap energies, are explored in detail. At least two main Eu^{3+} centers whose optical activation depends on both AlN nominal content and annealing temperature are identified. The temperature dependence of this emission is evaluated in order to explore its thermal stability in these nanostructures. The contribution of the GaN/AlN interface to the optical activation of these centers is also highlighted.

2. EXPERIMENTAL SECTION

The $Al_xGa_{1-x}N$ NWs with different AlN nominal content, x ($0 \leq x \leq 1$), were grown in nitrogen-rich conditions by plasma-assisted molecular beam epitaxy (PA-MBE) on Si (111) substrates. The substrate temperature was varied between 850-930 ℃ depending on x; the substrate was continuously rotated to promote homogeneous NW growth [55]. A 3 nm-thick AlN buffer layer was deposited prior to NW growth to improve their vertical orientation [56]. The GaN NW template was grown on the AlN buffer layer, followed by the growth of $Al_xGa_{1-x}N$ NW sections [57]. The obtained NW structure (Fig. 1*a*), in terms of density and dimensions of each section, depends on x, as indicated in Table 1. The existence of fluctuations in the AlN molar fraction along the growth axis (*c*-axis) was demonstrated in these NWs, and it was found to dominate the structural and optical properties of $Al_xGa_{1-x}N$ NWs at the nanoscale [57–60].

Eu^{3+}-implantation was realized at room temperature (RT) using 300 keV Eu^{3+} ions with a fluence of 10^{14} cm^{-2} at a tilt angle of 45º with respect to the *c*-axis (Fig. 1*a*). During implantation, the samples were rotated for a more homogeneous distribution of Eu^{3+} ions and implantation-induced defects [25,61]. Such implantation geometry favors that Eu^{3+} ions are mostly incorporated in the $Al_xGa_{1-x}N$ top-section, being their insertion in GaN NW template unlikely to occur due to shadowing effects caused by the high density of NWs and their longitudinal dimensions.

Monte Carlo simulations, obtained by SRIM 2013 code [62], predict a projected range of ~40 nm and ~55 nm, for GaN and AlN respectively (maximum Eu^{3+} concentration ~$2.3\text{-}2.5\times10^{19}$ cm^{-3}). It is important to note that SRIM does not consider the three-dimensionality of the NWs and therefore the projected range may be slightly different. Indeed, unlike layered structures for which the ions only impinge on the top facet, for oblique incidence the ions can impinge on the sidewall facets of the NWs, causing a higher estimated doped thickness than predicted by SRIM.

Post-implantation rapid thermal annealing (RTA) was carried out for $Al_xGa_{1-x}N$ ($x > 0$) NWs during 30 seconds under nitrogen (N_2) flow at 1000 ℃ and 1200 ℃. For GaN NWs ($x = 0$), RTA was performed at 1000 ℃ only, since higher annealing temperatures may induce severe damage in GaN due to nitrogen out-diffusion [63]. A common strategy to protect GaN for annealing temperatures above 1000 ℃ is the use of an AlN cap layer [64,65]. Thus, by annealing $Al_xGa_{1-x}N$ ($x > 0$) NWs at 1200 ℃, it is not expected to strongly damage the GaN NW template, as it is protected by the $Al_xGa_{1-x}N$ top-section [57]. Similar annealing conditions were reported to successfully achieve the recovery of the lattice damage introduced by the implantation and the optical activation of RE^{3+} ions in III-N layers [66,67] and nanostructures [26–28].

Table 1 summarizes the $Al_xGa_{1-x}N$ NWs studied in this work, and the used Eu^{3+}-implantation and RTA conditions. The samples' labels and their structural characteristics (NWs density and dimensions of each section) are also included.

Table 1. Structural characteristics of the $Al_xGa_{1-x}N$ NWs studied in this work: typical length (*h* in nm), average diameter (*d* in nm), and NWs density (cm^{-2}). (N/A: not applicable).

$Al_xGa_{1-x}N$		***x* = 0**	***x* = 0.3**	***x* = 0.5**	***x* = 0.75**	***x* = 1**
$Al_xGa_{1-x}N$-asgr (as-grown)						
$Al_xGa_{1-x}N$ NWs top-section	*d*	N/A	~35	~40	~45	~175
	h		~225	~260	~225	~500
GaN NW template	*d*		~35	~40	~35	~75
	h		< 200	< 200	< 200	~1500
GaN NWs	*d*	~35	N/A			
	h	~750				
NWs density		$\sim 1.5\times10^{10}$	$\sim 2.5\times10^{10}$			$\sim 5\times10^{9}$
Eu^{3+}-implantation		**$Al_xGa_{1-x}N$-asimp (as-implanted)**				
		Eu^{3+} fluence of 10^{14} cm^{-2}, 300 keV, 45º tilt *vs c*-axis				
Rapid thermal annealing (RTA)		**$Al_xGa_{1-x}N$-1000**				
		RTA at 1000 ℃ for 30 s in N_2 ambient				
		$Al_xGa_{1-x}N$-1200				
		N/A	RTA at 1200 ℃ for 30 s in N_2 ambient			

Scanning electron microscopy (SEM) of the $Al_xGa_{1-x}N$-asgr samples was performed using a Zeiss Ultra-55 system. Figs. 1*b* and 1*c* show representative SEM images of the $Al_{0.3}Ga_{0.7}N$-asgr NWs in side-view and top-view, respectively. In Fig. S1 (Supplementary Information), representative SEM images for the other NWs are depicted. Due to their density and dimensions, the vertical NWs exhibit partial coalescence caused by their bundling, as reported by Kaganer *et al*. for GaN NWs [68]. Radial growth of the $Al_xGa_{1-x}N$ NWs top-section is observed for high AlN nominal contents (Fig. S1*e* for $x = 0.75$, and Fig. S1*g* for $x = 1$ in Supplementary Information) due to limited diffusion of Al atoms along the sidewalls towards the top [69]. This effect also contributes to the coalescence of the NWs at the top-section. Moreover, substrate surface coverage (fill factor) is lower for $Al_xGa_{1-x}N$ NWs ($0 < x < 1$) in comparison to AlN NWs (Figs. S1*d*, S1*f*, and S1*h* in Supplementary Information), which reduces the shadowing effects during Eu^{3+}-implantation and increases the probability of Eu^{3+} to reach the GaN NW template.

RT μ-Raman measurements (Horiba Jobin-Yvon HR800) were performed on $Al_xGa_{1-x}N$ NW ensemble (beam spot ~1 μm^2), under 441.6 nm excitation line (He-Cd laser) in backscattering geometry $z(x,\cdot)\bar{z}$ to reduce the Si (111) substrate contribution. The beam was focused using a ×100 magnification objective ($NA = 0.9$, $f = 0.1$ cm).

PL measurements were carried out on $Al_xGa_{1-x}N$ NW ensemble (beam spot ~5 mm^2) using the 325 nm (3.8 eV) excitation line (He-Cd laser) with an excitation power density of about 0.5 W/cm^2.

Such energy allows above bandgap excitation for GaN NWs ($x = 0$) and below bandgap excitation for $Al_xGa_{1-x}N$ NWs ($x \geq 0.3$ in our samples). The PL signal was measured in a dispersive system SPEX 1704 monochromator (1 m, 1200 grooves/mm) coupled to a water-cooled Hamamatsu R928 photomultiplier tube. The samples were mounted in a cold finger of a closed-cycle helium cryostat and the temperature was controlled between 14 K and 300 K.

CL measurements were conducted on AlN-1000 and $Al_xGa_{1-x}N$-1200 ($x > 0$) NW ensembles (beam spot ~2 μm^2), at 5 K, under 5 kV acceleration voltage. The electron beam leads to the excitation of all the luminescence mechanisms present in the material, especially the creation of electron-hole pairs allowing above bandgap excitation.

It is important to mention that in CL, PL, and μ-Raman measurements, the average optical response of a few hundreds of NWs is collected simultaneously. Furthermore, a 5 kV acceleration voltage used in CL measurements results in a lower penetration depth compared to PL. In other words, the CL response comes predominantly from the NWs top-section (~70-190 nm), while the PL optical response is mainly from the $GaN/Al_xGa_{1-x}N$ interface and the GaN NWs template (up to ~80 nm below the interface) due to the lower absorption of the used laser line in the $Al_xGa_{1-x}N$ NWs top-section for $x > 0$.

Additionally, AlN-1200 NWs were dispersed on a foreign Si substrate, allowing nano-CL measurements on individual NWs, at 5 K, under 10 kV acceleration voltage.

3. RESULTS AND DISCUSSION

3.1. Structural and vibrational properties

Wurtzite (WZ) III-N semiconductors belong to the C_{6v}^4 space group with four atoms in the primitive cell, occupying C_{3v} sites. At the Brillouin zone (BZ) center, **q** = 0, six optical modes are active in first-order Raman scattering processes A_1(TO), A_1(LO), E_1(TO), E_1(LO), E_2^H, and E_2^L. In the backscattering configuration $z(x,\cdot)\bar{z}$, E_2^L, E_2^H, and A_1(LO) phonons are allowed according to the selection rules [70]. For ternary alloys such as $Al_xGa_{1-x}N$, A_1(LO) is characterized by a one-mode behavior (phonon frequency varies continuously from the A_1(LO) of one end binary to that of the other one with the mode strength remaining almost constant), while E_2^H exhibits a two-mode behavior (two impurity modes: E_2^H (GaN-like) and E_2^H (AlN-like), close to the frequency of the respective binaries), which blueshifts with x [71–73]. Nevertheless, it is important to consider that their behavior could be influenced by strain and compositional effects, while E_2^H (GaN-like) could also be affected by the possible superposition with the alloy E_1(TO) phonon [71–73].

Fig. 2*a* illustrates representative normalized μ-Raman spectra of the $Al_{0.3}Ga_{0.7}N$-(asgr, asimp, 1000, and 1200) NWs. The calculated phonon density of states (DOS) for GaN and the disorder-induced Raman spectrum for erbium (Er)-implanted AlN layers are included for comparison [74]. Fig. S2 (Supplementary Information) depicts the μ-Raman response of all the samples acquired in the same conditions. It should be mentioned that the allowed A_1(LO) phonon was not detected in these experiments. Except for AlN-asgr presenting E_2^H (GaN) and E_2^H (AlN), $Al_xGa_{1-x}N$-asgr exhibit an asymmetric response in the E_2^H (GaN) region (blue rectangle in Fig. 2*a* and Fig. S3*a*). The presence of this asymmetry (to higher frequencies) and its higher full width at half maximum (FWHM) when compared to E_2^H (GaN) of the binary, suggest more than one contribution. For $Al_{0.3}Ga_{0.7}N$-asgr, such response can be deconvoluted into two phonons (section S2.2. in Supplementary Information): E_2^H (GaN) at 568 cm^{-1} associated with the GaN NW

template and E_2^H (GaN like) at 571 cm^{-1} related to the alloy top-section. The resulting active phonons for all the samples are summarized in Fig. 2*b* and Table S1 (Supplementary Information).

We found that all $Al_xGa_{1-x}N$-asgr samples exhibit the E_2^H (GaN) phonon at 567-568 cm^{-1} (experimental error of ±1 cm^{-1}) indicating that both GaN-asgr NWs and GaN NW template are nearly-relaxed on Si (111) substrate (dotted line in Fig. 2*b* indicates the strain-free value of 567.6 cm^{-1} [74]). For $Al_xGa_{1-x}N$-asgr (x = 0.3, 0.5, and 0.75), the E_2^H (GaN-like) phonon (within the dashed rectangle in Fig. 2*b*) is composed of one or two components, indicating possible compositional fluctuations within the same NW or in different NWs, as discussed in other works [57,75]. $Al_xGa_{1-x}N$-asgr E_2^H (GaN-like) frequencies are found to be lower than the ones obtained for $Al_xGa_{1-x}N$ layers [73], which can be due to *i*) the tensile strain introduced by the growth of $Al_xGa_{1-x}N$ on the GaN NW template, and/or *ii*) the lower AlN content compared to the nominal value. For the AlN-asgr, the E_2^H (AlN) phonon located at 655 cm^{-1}, is slightly redshifted with respect to the strain-free value (657.4 cm^{-1} [74]), evidencing a tensile strain in the AlN section as a result of their growth on GaN NW template with higher *in-plane* lattice parameter (a_{GaN} = 3.189 Å and a_{AlN} = 3.112 Å [76]).

After Eu^{3+}-implantation, the lattice damage induces a higher absorption in the affected region. Thus, the μ-Raman signal (double absorption in backscattering geometry) and the signal-to-noise ratio (SNR) are strongly reduced. The μ-Raman spectra of the $Al_{0.3}Ga_{0.7}N$-asimp (Fig. 2*a*) exhibits disorder-activated second-order Raman scattering processes involving phonons from the entire BZ. As a result, the feature located at the E_2^H phonon mode shows an asymmetry at the low-frequency side (orange rectangle in Fig. 2*a*), while the asymmetry is observed at the high-frequency side in $Al_{0.3}Ga_{0.7}N$-asgr. A thorough analysis in the E_2^H (GaN) region reveals the presence of a strain-free E_2^H (GaN) phonon originating from the GaN NW template region not affected by Eu^{3+}-implantation, and an additional contribution located at 562 cm^{-1} from the GaN NW template region affected by Eu^{3+}-implantation (detailed in section S2.2. in Supplementary Information). The decrease of the E_2^H (GaN-like) contribution confirms that the $Al_xGa_{1-x}N$ top-section is the most affected by Eu^{3+}-implantation. One can notice that a similar behavior is obtained for $Al_xGa_{1-x}N$-asimp (with $0.3 < x < 1$). When it comes to AlN-asimp, the E_2^H (GaN) phonon originating from the GaN NW template keeps the same frequency, while the E_2^H (AlN) experiences a redshift (Fig. S2*b* in Supplementary Information), indicating that Eu^{3+}-implantation affects the AlN top-section. The obtained phonon redshift can be associated with hydrostatic tensile stress within the implanted volume, in good agreement with X-ray diffraction and molecular dynamics results on RE-implanted GaN NWs [25,77,78]. In GaN-asimp and AlN-asimp, we have estimated *quasi*-hydrostatic tensile stress ($\sigma_{xx} \approx \sigma_{yy} \approx \sigma_{zz}$) of ~1 GPa (section S2.3. in Supplementary Information).

After annealing, $Al_{0.3}Ga_{0.7}N$ NW ensemble shows a μ-Raman response dominated by first-order scattering processes at the BZ center (Fig. 1*a*), similar to the one of the $Al_{0.3}Ga_{0.7}N$-asgr. This result, together with an improved SNR for the highest annealing temperature, is consistent with a recovery of the as-grown crystalline structure. Furthermore, we confirm that the implantation-induced tensile stress gradually decreases after annealing for the binaries (Fig. S4 in Supplementary Information).

3.2. Emission properties

3.2.1. Above bandgap excitation of $Al_xGa_{1-x}N$-1200 (x > 0)

While the Eu^{3+} free ion intra-4f^6 transitions, such as from $^5D_{J\,(J=0,1,2)}$ to $^7F_{J\,(J=0\text{-}6)}$ multiplets, are forbidden by electric dipole according to Laporte selection rules, they happen to be partially allowed when the ions are introduced in a host material, since the crystal-field perturbation leads to the admixture of states with different parities [79,80]. Besides, crystal-field perturbation together with 4*f* electron spin-orbit coupling and electrostatic interaction contribute to the splitting of the energy levels in different Stark levels [81]. In III-N hosts, Eu^{3+} ions likely incorporate into cation substitutional sites (C_{3v} symmetry) [82], which leads to $^7F_1$ and $^7F_2$ multiplets splitting into two (one doublet and one singlet) and three (two doublets and one singlet) distinct levels, respectively. Slightly different Eu^{3+} environments (*e.g.*, substitutional cation site surrounded by cation/anion vacancies) can lower the symmetry and lift the degeneracy [44,81,83], reaching a maximum number of three and five levels for the $^7F_1$ and $^7F_2$ multiplets, respectively. The $^5D_0 \rightarrow {}^7F_0$ transition is characterized by its singlet character, *i.e.* no crystal field splitting is allowed for $^5D_0$ and $^7F_0$ levels, implying that the number of the observed $^5D_0 \rightarrow {}^7F_0$ transitions corresponds to the number of non-equivalent active sites if accidental overlaps are not considered [32,44,81,83,84].

Fig. 3*a* represents 5 K CL spectra of $Al_xGa_{1-x}N$-1200 NW ensembles ($x > 0$) with well-resolved characteristic sharp luminescence lines of the Eu^{3+} intra-4f^6 shell transitions, for which the most intense emission corresponds to the $^5D_0 \rightarrow {}^7F_2$ transition. The intensity of each spectrum was normalized to the corresponding $^5D_0 \rightarrow {}^7F_2$ transition. The observation of intra-4f^6 shell transitions indicates that the implantation and annealing conditions successfully achieved the activation of the Eu^{3+} ions in these hosts. The CL spectra magnified around the intra-4*f* transitions are shown in Figs. S5*a*-S5*f* (Supplementary Information). Table S2 (Supplementary Information) summarizes the Eu^{3+} peaks extracted and the corresponding assignments. Fig. 3*b* shows a magnification around the $^5D_0 \rightarrow {}^7F_0$ transition for the AlN-1200 sample and reveals that at least two non-equivalent active sites (590.2 nm – shoulder and 590.4 nm) are formed. The possible presence of a third Eu^{3+} peak (broad peak at 591.8 nm) cannot be discarded.

The evolution of the integrated CL intensity of the $^5D_0 \rightarrow {}^7F_2$ transition as a function of AlN nominal content is represented in Fig. 3*c*. For $Al_xGa_{1-x}N$-1200 ($0 < x < 1$), the intensity is similar independently on *x*, while for $x = 1$, it increases by an order of magnitude. This may be explained by the higher intensity ratio $I_{^5D_0 \rightarrow {}^7F_2}/I_{^5D_1 \rightarrow {}^7F_1}$ found for AlN-1200, suggesting a higher radiative recombination probability from the excited state $^5D_0$ instead of $^5D_1$ for the Eu^{3+}-implanted AlN NWs. Since luminescence properties are affected by the host's crystalline quality, a higher $^5D_0 \rightarrow {}^7F_2$ CL intensity for AlN-1200 might indicate a lower structural damage inflicted by ion implantation. Furthermore, when comparing the integrated intensity of the $^5D_0 \rightarrow {}^7F_2$ transition for AlN-1200 and AlN-1000 (also included in Fig. 3*c*), the value is doubled for the highest annealing temperature. This result demonstrates that the annealing temperature is a crucial parameter for the optimization of the Eu^{3+} emission and the efficient recovery of the as-grown crystalline properties.

In order to localize the Eu^{3+} emission in the NWs with the highest CL intensity, nano-CL was performed on dispersed AlN-1200 NWs. Fig. 4*a* shows the SEM image of the dispersed NWs (Fig. 4*a*) consisting of two coalesced NWs at the AlN top-section. Nano-CL intensity maps integrated at distinct central energies 4.722 eV (262 nm, Fig. 4*b*), 3.404 eV (364 nm, Fig. 4*c*), and 1.989 eV (624 nm, Fig. 4*d*) are also shown. The choice of the central energy of 4.722 eV comes directly from the AlN-1200 CL spectrum (Fig. S6 in Supplementary Information), which cannot be associated with AlN near band edge (NBE) expected to be > 6 eV, but with defects emission from AlN [85,86]. In turn, 3.404 eV corresponds to the NBE emission from GaN NW template.

The NW heterostructure consisting of an AlN NW top-section and GaN NW template is clearly resolved in Fig. 4. In this analysis, it is important to mention that the spatial localization of recombination processes is dependent on the carrier diffusion length, which is about 70 nm for electrons in GaN NWs [87]. Fig. 4*d* indicates that the distribution of optically active Eu^{3+} centers is preponderant in two regions: AlN top-section and GaN/AlN interface, with the latter revealing the most intense Eu^{3+} emission at 1.989 eV.

As mentioned above, when incorporated in III-N hosts, Eu^{3+} ions tend to occupy cation substitutional, or near-substitutional, lattice sites, which favor the achievement of the trivalent charge state Eu^{3+}. Depending on the surrounding environment, two dominant optically active Eu^{3+} centers are observed in GaN hosts and are usually identified as Eu1 and Eu2 [30,88]. Mitchell *et al*. ascribed Eu1 (at higher energy) and Eu2 (at lower energy) to complex defects involving substitutional Ga sites (Eu_{Ga}) and different next-neighbors in the crystalline lattice: nitrogen vacancies (V_N) and cation vacancies (V_{Ga}), respectively [89]. Theoretical studies revealed that these complexes have a stable configuration [90]. Additionally, it was demonstrated that electrical excitation of GaN:Eu devices favors the excitation of the Eu2 center (also labeled as OMVPE7) [35,91]. In fact, ion implantation might induce a high concentration of cation and nitrogen vacancies (V_{III} and V_N), leading to the incorporation of Eu^{3+}ions in cation sites and to the formation of complexes with the generated point defects, which can provide energetic levels within the host's bandgap able to assist Eu^{3+} excitation. Recently, two dominant optically active Eu^{3+} centers (Eu1 and Eu2) were identified by photoluminescence in Eu^{3+}-implanted AlN NWs, with similar spectral shape to the corresponding Eu1 and Eu2 centers in GaN [26].

Warnick *et al*. determined theoretically the migration barriers for V_{III} and V_N in GaN and $Al_{0.3}Ga_{0.7}N$. In strain-free GaN, the energetic barriers of V_N and V_{Ga} were found to be similar, while in $Al_{0.3}Ga_{0.7}N$, the migration energy was found higher for V_N and lower for V_{III} compared to GaN. When $Al_{0.3}Ga_{0.7}N$ samples are subjected to strain, the migration barriers for V_{III} are reduced, while V_N barriers keep the same value. Since the diffusion rate increases exponentially with the decrease of the migration barrier energy, the mobility of V_{III} is higher in strained regions, as is the case of the GaN/AlN interface [92]. Moreover, the annealing process necessary to optically activate the Eu^{3+} ions leads to a reorganization of the crystalline lattice, allowing not only the a reduction of the density of defects introduced by implantation but also the diffusion to energetically favorable locations [92]. Therefore, as indicated in Fig. 4*d*, the regions corresponding to AlN NW top-section and GaN/AlN interface can affect the optical properties of the Eu^{3+} ions differently, because of the different surrounding environment, the lattice and defects dynamics after implantation and annealing.

3.2.2. Above and below bandgap excitation: the $^5D_0 \rightarrow {}^7F_2$ transition

Fig. 5*a* displays a magnification of the 5 K CL and 14 K high-resolution (HR) PL spectra for $Al_xGa_{1-x}N$-1200 ($x > 0$) NW ensembles around the most intense transition, $^5D_0 \rightarrow {}^7F_2$. For the annealing temperature of 1000 ℃, HR PL spectra for $Al_xGa_{1-x}N$-1000 NW ensembles is shown in Fig. 5*b*. On the one hand, CL enables above bandgap excitation of $Al_xGa_{1-x}N$ for which the Eu^{3+} emission is possible through all the excitation mechanisms. On the other hand, PL obtained using 3.8 eV laser excitation, *i. e.* below $Al_xGa_{1-x}N$ ($x \geq 0.3$ in our samples) bandgap energy, Eu^{3+} emission can be achieved through direct and indirect processes. In a direct process, the excitation is resonant with an excited electronic state of the ion (4*f* or 5*d*), while indirect processes occur by energy-transfer (ET) from the host to the 4*f* electrons subsystem through non-radiative Auger-type

mechanisms. These mechanisms have been discussed by different authors for GaN-based layered structures [18,93–95]. Following Lozykowski *et al*. [95], the most probable excitation mechanism occurs through ET from excitons bound to isovalent traps to 4*f* electrons created by RE ions. Fig. 5*c* describes the defect-trap mediated ET model for the excitation/emission of Eu^{3+} ions in $Al_xGa_{1-x}N$ NWs. For above bandgap excitation (GaN NWs), two mechanisms are possible: *i*) creation of excitons in the host followed by their localization at the defect-traps; and *ii*) localization of one of the carriers at the defect-traps, and subsequently the localization of the other. In both cases, a non-radiative recombination and ET leaves 4*f* electrons in an excited state, resulting in intra-4*f* emission. For below bandgap excitation ($Al_xGa_{1-x}N$ NWs, $x \geq 0.3$) only the second mechanism is allowed.

As mentioned above for AlN-1200, at least two $^5D_0 \rightarrow {}^7F_0$ transitions were observed (Fig. 3*b*), indicating that at least two optically active centers are involved, as also confirmed by the different relative intensities of the most intense $^5D_0 \rightarrow {}^7F_2$ three peaks in PL and CL (Fig. 5*a*). Moreover, it is possible to observe that PL favors Eu2 in comparison to CL, *i.e.* the ratio I_{Eu2}/I_{Eu1} is higher in the PL spectrum. This agrees with the nano-CL results since the central energy of 1.989 eV corresponds to the Eu2 center and its optical contribution is higher at the interface GaN/AlN (Fig. 4*d*). We remind that the CL response of the NW ensemble comes predominantly from the NWs top-section, while the PL experiments provide information not only from the NWs top-section but also from the GaN/$Al_xGa_{1-x}N$ interface and the GaN NW template.

For $Al_{0.5}Ga_{0.5}N$-1200, CL and PL spectra show nearly identical luminescence response, while for $Al_xGa_{1-x}N$-1200 (with x = 0.3 and 0.75), these spectra exhibit similar shape with slightly different peaks' resolution and energy, which can be associated with compositional fluctuations in the NWs and different resolution of both techniques. Alloy disorder and/or compositional fluctuations felt by the RE ions also contribute to the increase of the broadening of the $^5D_0 \rightarrow {}^7F_2$ emission [18,51,67]. A tentative representation of the spectral shape evolution with the AlN nominal content is shown in Fig. 5*d*. Here, the lower (higher) energy center Eu1 (Eu2) contribution is represented with luminescence intensities of I_{Eu1} (I_{Eu2}). When considering such representation, the ratio I_{Eu2}/I_{Eu1} is found to decrease when x increases. For the annealing temperature of 1200 ℃, it is possible to tune the Eu^{3+} optical active center by changing the nominal AlN content, which verifies that the relative abundance of the Eu^{3+} centers is extremely sensitive to the surrounding environment.

The annealing temperature is a parameter of utmost importance for device development and performance because it can affect the contribution of the different Eu^{3+} centers [30], as defined here by the ratio I_{Eu2}/I_{Eu1}. Furthermore, it was demonstrated that the electrical properties of Eu^{3+}-implanted/annealed diode structure degrade when subjected to high temperature and high pressure annealing at 1400 ℃ [47]. For GaN:Eu^{3+} layers capped with AlN, it was reported that the Eu2 center is predominant for annealing temperatures of 1300 ℃ [88], while an opposite behavior was recently reported in AlN:Eu^{3+} NWs showing that Eu2 is favored for rapid thermal annealing treatments at 1000 ℃ [26]. Therefore, the evaluation of the impact of the annealing temperature in the Eu^{3+} emission is needed. To do so, the behavior of the $^5D_0 \rightarrow {}^7F_2$ transition for the $Al_xGa_{1-x}N$-1000 NW ensembles is explored as a function of x and its behavior compared to that of the $Al_xGa_{1-x}N$-1200 samples. For the $Al_xGa_{1-x}N$-1000 (Fig. 5*b*), the behavior of the Eu^{3+} active center, shows an opposite trend when compared to the one observed for $Al_xGa_{1-x}N$-1200 NWs. In fact, while GaN-1000 and $Al_{0.3}Ga_{0.7}N$-1000 show a higher contribution of the Eu1 center (*i.e.* $I_{Eu2}<I_{Eu1}$), the contribution of the Eu2 increases for AlN-1000, which indicates that the ratio I_{Eu2}/I_{Eu1} increases when x increases. Note that for $Al_{0.5}Ga_{0.5}N$-1000 and $Al_{0.75}Ga_{0.25}N$-1000

samples, the emission exhibits a shoulder at the high-energy side (grey rectangle in Fig. 5*b*) that could be associated with GaN NW template (detailed in section S3.3 in Supplementary Information).

Moreover, as seen in Fig. 6, a redshift of the $^5D_0 \rightarrow {}^7F_2$ transition components is observed when *x* increases, in agreement with reports on $Al_xGa_{1-x}N:Eu^{3+}$ layers [18,29,51]. This shift is due to the higher expansion of the 4*f*-orbitals in AlN caused by the larger electron affinity of Al compared to Ga [51].

3.2.3. Below bandgap excitation: temperature dependence of $^5D_0 \rightarrow {}^7F_2$ transition

Temperature-dependent HR PL measurements at 14 K and 300 K are shown for $Al_{0.3}Ga_{0.7}N$-(1000, 1200) and AlN-(1000, 1200) samples (Figs. 7*a* and 7*b*, respectively). The evolution for all the temperatures and all the implanted samples are shown in Fig. S8 (Supplementary Information). The optical center Eu1 (Eu2) is highlighted with violet (orange) dashed line. When increasing the temperature from 14 K to 300 K, the PL spectra become less resolved due to the phonon broadening, rendering the distinction of the optically active Eu^{3+} centers even more difficult. In addition, competitive thermally-induced non-radiative processes cause an overall decrease of the Eu^{3+} intensity (Figs. 7*a*, 7*b* and S8). Such thermal quenching results from the ET to either radiative and/or non-radiative defects in the vicinity of each Eu^{3+} center. Moreover, for AlN hosts, the ratio I_{Eu2}/I_{Eu1} decreases with temperature, indicating that Eu1 is thermally more stable. For the ternaries, the peak broadening renders the identification of such behavior more difficult. The different quenching behaviors of $Al_xGa_{1-x}N$-1000 and $Al_xGa_{1-x}N$-1200 NW ensembles is better seen in Fig. 7*c* which represents the evolution of the ratio of the $^5D_0 \rightarrow {}^7F_2$ integrated PL intensity at 300 K and 14 K, $I_{300\ K}/I_{14\ K}$, versus *x*. For the annealing temperature of 1000 °C, we note that the thermal quenching is lower for the ternary alloys when compared to GaN-1000 NWs and characterized by $I_{300\ K}/I_{14\ K}$ ~50%. The fact that a strong quenching is present in the $Al_xGa_{1-x}N$-1000 (with $x > 0.5$) NWs can be tentatively associated with the predominance of the Eu2 center, which is highly sensitive to temperature in AlN hosts. However, the thermal quenching is reduced for $Al_xGa_{1-x}N$-1200 NWs when the AlN nominal content increases, reaching its maximum for AlN-1200 NWs and characterized by the highest $I_{300\ K}/I_{14\ K}$ value of ~80%. This effect can be explained by the higher contribution of the thermally stable Eu1 center with respect to the Eu2 center for the annealing temperature of 1200 °C.

4. CONCLUSIONS

To summarize and conclude, the incorporation of Eu^{3+} ions in implanted and annealed $Al_xGa_{1-x}N$ NWs was studied by μ-Raman and nano-CL, being observed that the $Al_xGa_{1-x}N$ top-section is the most affected region. A partial recovery of the implantation-induced damage was obtained after RTA as confirmed by μ-Raman. RTA also provided the optical activation of the Eu^{3+} ions, being possible to be excited with above (CL) and below (PL) bandgap energies. The $^5D_0 \rightarrow {}^7F_2$ transition is the most intense and its energy redshifts from GaN to AlN NWs. It was found that its spectral shape depends on two effects: AlN nominal content and annealing temperature, indicating that such behavior is attributed to at least two optically active Eu^{3+} centers (Eu1 and Eu2). In this sense, the ratio I_{Eu2}/I_{Eu1} increases with *x* for the lower annealing temperature while the opposite trend is verified for the higher annealing temperature. In addition, temperature-dependent PL evidenced a thermal quenching of the Eu^{3+} luminescence, for which AlN-1200 NWs show the lowest

quenching ($I_{300\,K}/I_{14\,K}$ value of ~80 %) compared to the rest of the samples. Thus, the interplay between the AlN nominal content and the annealing temperature can be used to tune the optical contribution of Eu^{3+} centers in $Al_xGa_{1-x}N$ NWs. This significant result can help to optimize the optical activation of Eu^{3+} centers in III-N semiconductors since some of them are favored under electrical excitation for red light-emitting diodes. Therefore, it can be a viable route to improve the efficiency of these devices.

ASSOCIATED CONTENT

Supplementary Material Complementary experiments including scanning electron microscopy images and μ-Raman response of $Al_xGa_{1-x}N$ NWs, deconvolution procedure of E_2^H (GaN) and E_2^H (GaN-like) phonons, determination of hydrostatic strain in GaN and AlN NWs, CL and PL response of the $Al_xGa_{1-x}N$ NWs, peak assignment of the Eu^{3+} intra-$4f^6$ transitions, and heterogeneity of the $Al_xGa_{1-x}N$ NWs and its impact on the Eu^{3+} emission.

CONFLICT OF INTEREST

The authors declare that they have no known financial/commercial Conflict of Interest.

ACKNOWLEDGMENTS

This work was supported by the project “Nano-engineering of wide bandgap semiconductors using ion beams” (NASIB) funded by FCT (Portuguese Foundation for Science and Technology) and FEDER (POCI-01-0145-FEDER-028011 and LISBOA-01-0145-FEDER-029666). This work was developed within the scope of the project I3N, UIDB/50025/2020 & UIDP/50025/2020, financed by national funds through the FCT/MEC. JC acknowledges the Ph.D. grant DAEPHYS-FCT PD/BD/142780/2018. GJ acknowledges the financial support of the program “Initiatives de Recherche Stratégiques” (IRS) of IDEX Univ. Grenoble Alpes (15-IDEX-0002)

REFERENCES

[1] N. Ben Sedrine, R. Ribeiro-Andrade, A. Gustafsson, M.R. Soares, J. Bourgard, J.P. Teixeira, P.M.P. Salomé, M.R. Correia, M.V.B. Moreira, A.G. De Oliveira, J.C. González, J.P. Leitão, Fluctuating potentials in GaAs:Si nanowires: critical reduction of the influence of polytypism on the electronic structure, Nanoscale. 10 (2018) 3697–3708. https://doi.org/10.1039/C7NR08395E.

[2] J. Rodrigues, N. Ben Sedrine, M.R. Correia, T. Monteiro, Photoluminescence investigations of ZnO micro/nanostructures, Mater. Today Chem. 16 (2020). https://doi.org/10.1016/j.mtchem.2020.100243.

[3] F. Ishikawa, I.A. Buyanova, eds., Novel Compound Semiconductor Nanowires: Materials, Devices, and Applications, Pan Stanford Publishing Pte. Ltd., Singapore, 2018.

[4] A.-L. Henneghien, G. Tourbot, B. Daudin, O. Lartigue, Y. Désières, J.-M. Gérard, Optical anisotropy and light extraction efficiency of MBE grown GaN nanowires epilayers, Opt. Express. 19 (2011) 527. https://doi.org/10.1364/OE.19.000527.

[5] A.Y. Polyakov, T. Kim, I. Lee, S.J. Pearton, III- Nitride Nanowires as Building Blocks for Advanced Light Emitting Diodes, Phys. Status Solidi. 256 (2019) 1800589. https://doi.org/10.1002/pssb.201800589.

[6] A. Yanagihara, K. Kishino, Red- Emitting InGaN- Based Nanocolumn Light- Emitting Diodes with Highly Directional Beam Profiles, Phys. Status Solidi. 217 (2020) 1900771. https://doi.org/10.1002/pssa.201900771.

[7] Y. Robin, S.Y. Bae, T. V. Shubina, M. Pristovsek, E.A. Evropeitsev, D.A. Kirilenko, V.Y. Davydov, A.N. Smirnov, A.A. Toropov, V.N. Jmerik, M. Kushimoto, S. Nitta, S. V. Ivanov, H. Amano, Insight into the performance of multi-color InGaN/GaN nanorod light emitting diodes, Sci. Rep. 8 (2018) 7311. https://doi.org/10.1038/s41598-018-25473-x.

[8] S.M. Sadaf, S. Zhao, Y. Wu, Y.-H. Ra, X. Liu, S. Vanka, Z. Mi, An AlGaN Core–Shell Tunnel Junction Nanowire Light-Emitting Diode Operating in the Ultraviolet-C Band, Nano Lett. 17 (2017) 1212–1218. https://doi.org/10.1021/acs.nanolett.6b05002.

[9] N. Guan, X. Dai, A. Messanvi, H. Zhang, J. Yan, E. Gautier, C. Bougerol, F.H. Julien, C. Durand, J. Eymery, M. Tchernycheva, Flexible White Light Emitting Diodes Based on Nitride Nanowires and Nanophosphors, ACS Photonics. 3 (2016) 597–603. https://doi.org/10.1021/acsphotonics.5b00696.

[10] S. Zhao, S.Y. Woo, M. Bugnet, X. Liu, J. Kang, G.A. Botton, Z. Mi, Three-Dimensional Quantum Confinement of Charge Carriers in Self-Organized AlGaN Nanowires: A Viable Route to Electrically Injected Deep Ultraviolet Lasers, Nano Lett. 15 (2015) 7801–7807. https://doi.org/10.1021/acs.nanolett.5b02133.

[11] S. Zhao, A.T. Connie, M.H.T. Dastjerdi, X.H. Kong, Q. Wang, M. Djavid, S. Sadaf, X.D. Liu, I. Shih, H. Guo, Z. Mi, Aluminum nitride nanowire light emitting diodes: Breaking the fundamental bottleneck of deep ultraviolet light sources, Sci. Rep. 5 (2015) 8332. https://doi.org/10.1038/srep08332.

[12] S. Albert, A.M. Bengoechea-Encabo, M.Á. Sánchez-García, E. Calleja, Selective Area

Growth of InGaN/GaN Nanocolumnar Heterostructures by Plasma-Assisted Molecular Beam Epitaxy, in: Semicond. Semimetals, 2017: pp. 231–266. https://doi.org/10.1016/bs.semsem.2016.08.003.

[13] M.S. Wong, S. Nakamura, S.P. DenBaars, Review—Progress in High Performance III-Nitride Micro-Light-Emitting Diodes, ECS J. Solid State Sci. Technol. 9 (2020) 015012. https://doi.org/10.1149/2.0302001jss.

[14] C. Zhou, A. Ghods, V.G. Saravade, P. V. Patel, K.L. Yunghans, C. Ferguson, Y. Feng, B. Kucukgok, N. Lu, I.T. Ferguson, Review—The Current and Emerging Applications of the III-Nitrides, ECS J. Solid State Sci. Technol. 6 (2017) Q149–Q156. https://doi.org/10.1149/2.0101712jss.

[15] O. Ambacher, J. Majewski, C. Miskys, A. Link, M. Hermann, M. Eickhoff, M. Stutzmann, F. Bernardini, V. Fiorentini, V. Tilak, B. Schaff, L.F. Eastman, Pyroelectric properties of Al(In)GaN/GaN hetero- and quantum well structures, J. Phys. Condens. Matter. 14 (2002) 3399–3434. https://doi.org/10.1088/0953-8984/14/13/302.

[16] A. Koizumi, K. Kawabata, D. Lee, A. Nishikawa, Y. Terai, H. Ofuchi, T. Honma, Y. Fujiwara, In situ Eu doping into $Al_xGa_{1-x}N$ grown by organometallic vapor phase epitaxy to improve luminescence properties, Opt. Mater. (Amst). 41 (2015) 75–79. https://doi.org/10.1016/j.optmat.2014.11.005.

[17] J.B. Gruber, U. Vetter, T. Taniguchi, G.W. Burdick, H. Hofsäss, S. Chandra, D.K. Sardar, Spectroscopic analysis of Eu^{3+} in single-crystal hexagonal phase AlN, J. Appl. Phys. 110 (2011) 023104. https://doi.org/10.1063/1.3609076.

[18] K. Wang, K.P. O'Donnell, B. Hourahine, R.W. Martin, I.M. Watson, K. Lorenz, E. Alves, Luminescence of Eu ions in $Al_xGa_{1-x}N$ across the entire alloy composition range, Phys. Rev. B. 80 (2009) 125206. https://doi.org/10.1103/PhysRevB.80.125206.

[19] T. Andreev, N.Q. Liem, Y. Hori, M. Tanaka, O. Oda, D.L.S. Dang, B. Daudin, Optical transitions in Eu^{3+} ions in GaN:Eu grown by molecular beam epitaxy, Phys. Rev. B - Condens. Matter Mater. Phys. 73 (2006) 3–8. https://doi.org/10.1103/PhysRevB.73.195203.

[20] T. Fujiwara, A. Wakahara, Y. Nakanishi, A. Yoshida, T. Oshima, T. Kamiya, Photoluminescence properties of Eu-implanted $Al_xGa_{1-x}N$ ($0 \leq x \leq 1$), Phys. Status Solidi. 2 (2005) 2805–2808. https://doi.org/10.1002/pssc.200461431.

[21] A.J. Steckl, J. Heikenfeld, D.S. Lee, M. Garter, Multiple color capability from rare earth-doped gallium nitride, Mater. Sci. Eng. B. 81 (2001) 97–101. https://doi.org/10.1016/S0921-5107(00)00745-5.

[22] J. Heikenfeld, M. Garter, D.S. Lee, R. Birkhahn, A.J. Steckl, Red light emission by photoluminescence and electroluminescence from Eu-doped GaN, Appl. Phys. Lett. 75 (1999) 1189–1191. https://doi.org/10.1063/1.124686.

[23] K. Wang, R.W. Martin, K.P. O'Donnell, V. Katchkanov, E. Nogales, K. Lorenz, E. Alves, S. Ruffenach, O. Briot, Selectively excited photoluminescence from Eu-implanted GaN, Appl. Phys. Lett. 87 (2005) 112107. https://doi.org/10.1063/1.2045551.

[24] H. Sekiguchi, K. Date, T. Imanishi, H. Tateishi, K. Yamane, H. Okada, K. Kishino, A. Wakahara, Regularly arranged Eu-doped GaN nanocolumns grown by RF-plasma-assisted molecular beam epitaxy through Ti-mask selective-area growth technique, J. Cryst. Growth. 511 (2019) 73–78. https://doi.org/10.1016/j.jcrysgro.2019.01.032.

[25] D.N. Faye, X. Biquard, E. Nogales, M. Felizardo, M. Peres, A. Redondo-Cubero, T. Auzelle, B. Daudin, L.H.G. Tizei, M. Kociak, P. Ruterana, W. Möller, B. Méndez, E. Alves, K. Lorenz, Incorporation of Europium into GaN Nanowires by Ion Implantation, J. Phys. Chem. C. 123 (2019) 11874–11887. https://doi.org/10.1021/acs.jpcc.8b12014.

[26] J. Cardoso, N. Ben Sedrine, A. Alves, M.A. Martins, M. Belloeil, B. Daudin, D.N. Faye, E. Alves, K. Lorenz, A.J. Neves, M.R. Correia, T. Monteiro, Multiple optical centers in Eu-implanted AlN nanowires for solid-state lighting applications, Appl. Phys. Lett. 113 (2018) 201905. https://doi.org/10.1063/1.5048772.

[27] J. Rodrigues, M.F. Leitão, J.F.C. Carreira, N. Ben Sedrine, N.F. Santos, M. Felizardo, T. Auzelle, B. Daudin, E. Alves, A.J. Neves, M.R. Correia, F.M. Costa, K. Lorenz, T. Monteiro, Spectroscopic Analysis of Eu^{3+} Implanted and Annealed GaN Layers and Nanowires, J. Phys. Chem. C. 119 (2015) 17954–17964. https://doi.org/10.1021/acs.jpcc.5b05101.

[28] J. Rodrigues, M.F. Leitão, J.F.C. Carreira, N. Ben Sedrine, N.F. Santos, M. Felizardo, T. Auzelle, B. Daudin, E. Alves, A.J. Neves, M.R. Correia, F.M. Costa, K. Lorenz, T. Monteiro, Correction to "Spectroscopic Analysis of Eu^{3+} Implanted and Annealed GaN Layers and Nanowires," J. Phys. Chem. C. 120 (2016) 6907–6908. https://doi.org/10.1021/acs.jpcc.6b02591.

[29] S. Magalhães, M. Peres, V. Fellmann, B. Daudin, A.J. Neves, E. Alves, T. Monteiro, K. Lorenz, Functionalizing self-assembled GaN quantum dot superlattices by Eu-implantation, J. Appl. Phys. 108 (2010) 084306. https://doi.org/10.1063/1.3496624.

[30] L. Bodiou, A. Braud, J.-L. Doualan, R. Moncorgé, J.H. Park, C. Munasinghe, A.J. Steckl, K. Lorenz, E. Alves, B. Daudin, Optically active centers in Eu implanted, Eu in situ doped GaN, and Eu doped GaN quantum dots, J. Appl. Phys. 105 (2009) 043104. https://doi.org/10.1063/1.3078783.

[31] H. Sekiguchi, T. Imanishi, R. Matsuzaki, K. Ozaki, K. Yamane, H. Okada, K. Kishino, A. Wakahara, Stable-wavelength operation of europium-doped GaN nanocolumn light-emitting diodes grown by rf-plasma-assisted molecular beam epitaxy, Electron. Lett. 53 (2017) 666–668. https://doi.org/10.1049/el.2017.0447.

[32] N. Ben Sedrine, J. Rodrigues, D.N. Faye, A.J. Neves, E. Alves, M. Bockowski, V. Hoffmann, M. Weyers, K. Lorenz, M.R. Correia, T. Monteiro, Eu-Doped AlGaN/GaN Superlattice-Based Diode Structure for Red Lighting: Excitation Mechanisms and Active Sites, ACS Appl. Nano Mater. 1 (2018) 3845–3858. https://doi.org/10.1021/acsanm.8b00612.

[33] A. Nishikawa, T. Kawasaki, N. Furukawa, Y. Terai, Y. Fujiwara, Room-Temperature Red Emission from a p-Type/Europium-Doped/n-Type Gallium Nitride Light-Emitting Diode under Current Injection, Appl. Phys. Express. 2 (2009) 071004. https://doi.org/10.1143/APEX.2.071004.

[34] A. Wakahara, H. Sekiguchi, H. Okada, Y. Takagi, Current status for light-emitting diode with Eu-doped GaN active layer grown by MBE, J. Lumin. 132 (2012) 3113–3117. https://doi.org/10.1016/j.jlumin.2012.02.001.

[35] M. Ishii, A. Koizumi, Y. Fujiwara, Nanoscale determinant to brighten up GaN:Eu red light-emitting diode: Local potential of Eu-defect complexes, J. Appl. Phys. 117 (2015) 155307. https://doi.org/10.1063/1.4918662.

[36] B. Mitchell, V. Dierolf, T. Gregorkiewicz, Y. Fujiwara, Perspective: Toward efficient GaN-based red light emitting diodes using europium doping, J. Appl. Phys. 123 (2018) 160901. https://doi.org/10.1063/1.5010762.

[37] A. Sukegawa, H. Sekiguchi, R. Matsuzaki, K. Yamane, H. Okada, K. Kishino, A. Wakahara, Self-Organized Eu-Doped GaN Nanocolumn Light-Emitting Diode Grown by RF-Molecular-Beam Epitaxy, Phys. Status Solidi. 216 (2018) 1800501. https://doi.org/10.1002/pssa.201800501.

[38] W. Zhu, B. Mitchell, D. Timmerman, A. Koizumi, T. Gregorkiewicz, Y. Fujiwara, High-Power Eu-Doped GaN Red LED Based on a Multilayer Structure Grown at Lower Temperatures by Organometallic Vapor Phase Epitaxy, MRS Adv. 2 (2017) 159–164. https://doi.org/10.1557/adv.2017.67.

[39] D. Timmerman, B. Mitchell, S. Ichikawa, J. Tatebayashi, M. Ashida, Y. Fujiwara, Excitation Efficiency and Limitations of the Luminescence of Eu^{3+} Ions in GaN, Phys. Rev. Appl. 13 (2020). https://doi.org/10.1103/PhysRevApplied.13.014044.

[40] P.N. Favennec, H. L'Haridon, M. Salvi, D. Moutonnet, Y. Le Guillou, Luminescence of erbium implanted in various semiconductors: IV, III-V and II-VI materials, Electron. Lett. 25 (1989) 718–719. https://doi.org/10.1049/el:19890486.

[41] K.P. O'Donnell, The temperature dependence of the luminescence of rare-earth-doped semiconductors: 25 years after Favennec, Phys. Status Solidi. 12 (2015) 466–468. https://doi.org/10.1002/pssc.201400133.

[42] N. Ben Sedrine, J. Rodrigues, J. Cardoso, D.N. Faye, M. Fialho, S. Magalhães, A.F. Martins, A.J. Neves, E. Alves, M. Bockowski, V. Hoffmann, M. Weyers, K. Lorenz, M.R. Correia, T. Monteiro, Optical investigations of europium ion implanted in nitride-based diode structures, Surf. Coatings Technol. 355 (2018) 40–44. https://doi.org/10.1016/j.surfcoat.2018.02.004.

[43] K. Lorenz, E. Alves, I.S. Roqan, R.W. Martin, C. Trager-Cowan, K.P. O'Donnell, I.M. Watson, Rare earth doping of III-nitride alloys by ion implantation, Phys. Status Solidi. 205 (2008) 34–37. https://doi.org/10.1002/pssa.200776714.

[44] T. Monteiro, C. Boemare, M.J. Soares, R.A. Sá Ferreira, L.D. Carlos, K. Lorenz, R. Vianden, E. Alves, Photoluminescence and lattice location of Eu and Pr implanted GaN samples, Phys. B Condens. Matter. 308–310 (2001) 22–25. https://doi.org/10.1016/S0921-4526(01)00656-1.

[45] K. O'Donnell, V. Dierolf, eds., Rare-Earth Doped III-Nitrides for Optoelectronic and Spintronic Applications, Springer, Dordrecht, The Netherlands, 2010.

[46] M. Peres, E. Nogales, B. Mendez, K. Lorenz, M.R. Correia, T. Monteiro, N. Ben Sedrine, Eu Activation in β-Ga_2O_3 MOVPE Thin Films by Ion Implantation, ECS J. Solid State Sci. Technol. 8 (2019) Q3097–Q3102. https://doi.org/10.1149/2.0191907jss.

[47] D.N. Faye, M. Fialho, S. Magalhães, E. Alves, N. Ben Sedrine, J. Rodrigues, M.R. Correia, T. Monteiro, M. Boćkowski, V. Hoffmann, M. Weyers, K. Lorenz, Study of damage formation and annealing of implanted III-nitride semiconductors for optoelectronic devices, Nucl. Instruments Methods Phys. Res. Sect. B Beam Interact. with Mater. Atoms. 379 (2016) 251–254. https://doi.org/10.1016/j.nimb.2016.03.028.

[48] K. Lorenz, E. Alves, T. Monteiro, A. Cruz, M. Peres, Structural and optical characterisation of Eu implanted $Al_xGa_{1-x}N$, Nucl. Instruments Methods Phys. Res. Sect. B Beam Interact. with Mater. Atoms. 257 (2007) 307–310. https://doi.org/10.1016/j.nimb.2007.01.020.

[49] S.O. Kucheyev, J.S. Williams, J. Zou, C. Jagadish, Dynamic annealing in III-nitrides under ion bombardment, J. Appl. Phys. 95 (2004) 3048–3054. https://doi.org/10.1063/1.1649459.

[50] S.O. Kucheyev, J.S. Williams, J. Zou, G. Li, C. Jagadish, M.O. Manasreh, M. Pophristic, S. Guo, I.T. Ferguson, Structural disorder in ion-implanted $Al_xGa_{1-x}N$, Appl. Phys. Lett. 80 (2002) 787–789. https://doi.org/10.1063/1.1445478.

[51] A. Wakahara, Impact of AlGaN on luminescence capability of rare-earth ions in AlGaN, Opt. Mater. (Amst). 28 (2006) 731–737. https://doi.org/10.1016/j.optmat.2005.09.011.

[52] Y. Nakanishi, A. Wakahara, H. Okada, A. Yoshida, T. Ohshima, H. Itoh, T. Shibata, M. Tanaka, Effects of Al composition on luminescence properties of europium implanted $Al_xGa_{1-x}N$ ($0 \leq x \leq 1$), Phys. Status Solidi. 96 (2003) 2623–2626. https://doi.org/10.1002/pssc.200303440.

[53] K. Lorenz, E. Wendler, A. Redondo-Cubero, N. Catarino, M.-P. Chauvat, S. Schwaiger, F. Scholz, E. Alves, P. Ruterana, Implantation damage formation in a-, c- and m-plane GaN, Acta Mater. 123 (2017) 177–187. https://doi.org/10.1016/j.actamat.2016.10.020.

[54] N. Catarino, E. Nogales, N. Franco, V. Darakchieva, S.M.C. Miranda, B. Méndez, E. Alves, J.G. Marques, K. Lorenz, Enhanced dynamic annealing and optical activation of Eu implanted a-plane GaN, EPL (Europhysics Lett. 97 (2012) 68004. https://doi.org/10.1209/0295-5075/97/68004.

[55] M. Belloeil, Molecular beam epitaxy growth and optical characterization of GaN/AlGaN nanowire heterostructures emitting in the ultraviolet, Doctoral dissertation, Université Grenoble Alpes, 2017.

[56] R. Songmuang, O. Landré, B. Daudin, From nucleation to growth of catalyst-free GaN nanowires on thin AlN buffer layer, Appl. Phys. Lett. 91 (2007). https://doi.org/10.1063/1.2817941.

[57] A. Pierret, C. Bougerol, S. Murcia-Mascaros, A. Cros, H. Renevier, B. Gayral, B. Daudin, Growth, structural and optical properties of AlGaN nanowires in the whole composition range, Nanotechnology. 24 (2013) 115704. https://doi.org/10.1088/0957-4484/24/11/115704.

[58] M. Belloeil, B. Gayral, B. Daudin, Quantum Dot-Like Behavior of Compositional

Fluctuations in AlGaN Nanowires, Nano Lett. 16 (2016) 960–966. https://doi.org/10.1021/acs.nanolett.5b03904.

[59] M. Belloeil, M.G. Proietti, H. Renevier, B. Daudin, Nanoscale x-ray investigation of composition fluctuations in AlGaN nanowires, Nanotechnology. (2020) 11–14. https://doi.org/10.1088/1361-6528/ab94e1.

[60] A. Pierret, C. Bougerol, M. den Hertog, B. Gayral, M. Kociak, H. Renevier, B. Daudin, Structural and optical properties of $Al_xGa_{1-x}N$ nanowires, Phys. Status Solidi - Rapid Res. Lett. 7 (2013) 868–873. https://doi.org/10.1002/pssr.201308009.

[61] C. Ronning, C. Borschel, S. Geburt, R. Niepelt, Ion beam doping of semiconductor nanowires, Mater. Sci. Eng. R Reports. 70 (2010) 30–43. https://doi.org/10.1016/j.mser.2010.07.002.

[62] J.F. Ziegler, J.P. Biersack, Matthias D. Ziegler, SRIM: The stopping and range of ions in matter, SRIM Co., Chester, Maryland, 2008. https://doi.org/10.1016/0306-4549(78)90039-7.

[63] I. Grzegory, S. Porowski, High pressure solution growth of GaN and related compounds, in: J.H. Edgar, S. Strite, I. Akasaki, H. Amano, C. Wetzel (Eds.), Prop. Process. Appl. Gall. Nitride Relat. Semicond., INSPEC, The Institution of Electrical Engineers, London, United Kingdom, 1998.

[64] E. Nogales, R.W. Martin, K.P. O'Donnell, K. Lorenz, E. Alves, S. Ruffenach, O. Briot, Failure mechanism of AlN nanocaps used to protect rare earth-implanted GaN during high temperature annealing, Appl. Phys. Lett. 88 (2006) 031902. https://doi.org/10.1063/1.2162797.

[65] K. Lorenz, U. Wahl, E. Alves, S. Dalmasso, R.W. Martin, K.P. O'Donnell, S. Ruffenach, O. Briot, High-temperature annealing and optical activation of Eu-implanted GaN, Appl. Phys. Lett. 85 (2004) 2712–2714. https://doi.org/10.1063/1.1801686.

[66] M. Fialho, J. Rodrigues, S. Magalhães, M.R. Correia, T. Monteiro, K. Lorenz, E. Alves, Effect of AlN content on the lattice site location of terbium ions in $Al_xGa_{1-x}N$ compounds, Semicond. Sci. Technol. 31 (2016) 035026. https://doi.org/10.1088/0268-1242/31/3/035026.

[67] J. Rodrigues, M. Fialho, S. Magalhães, M.R. Correia, L. Rino, E. Alves, A.J. Neves, K. Lorenz, T. Monteiro, Analysis of the Tb^{3+} recombination in ion implanted $Al_xGa_{1-x}N$ ($0 \leq x \leq 1$) layers, J. Lumin. 178 (2016) 249–258. https://doi.org/10.1016/j.jlumin.2016.05.018.

[68] V.M. Kaganer, S. Fernández-Garrido, P. Dogan, K.K. Sabelfeld, O. Brandt, Nucleation, Growth, and Bundling of GaN Nanowires in Molecular Beam Epitaxy: Disentangling the Origin of Nanowire Coalescence, Nano Lett. 16 (2016) 3717–3725. https://doi.org/10.1021/acs.nanolett.6b01044.

[69] R. Songmuang, T. Ben, B. Daudin, D. González, E. Monroy, Identification of III–N nanowire growth kinetics via a marker technique, Nanotechnology. 21 (2010) 295605. https://doi.org/10.1088/0957-4484/21/29/295605.

[70] C.A. Arguello, D.L. Rousseau, S.P.S. Porto, First-Order Raman Effect in Wurtzite-Type Crystals, Phys. Rev. 181 (1969) 1351–1363. https://doi.org/10.1103/PhysRev.181.1351.

[71] H. Grille, C. Schnittler, F. Bechstedt, Phonons in ternary group-III nitride alloys, Phys. Rev. B. 61 (2000) 6091–6105. https://doi.org/10.1103/PhysRevB.61.6091.

[72] M. Holtz, T. Prokofyeva, M. Seon, K. Copeland, J. Vanbuskirk, S. Williams, S.A. Nikishin, V. Tretyakov, H. Temkin, Composition dependence of the optical phonon energies in hexagonal $Al_xGa_{1-x}N$, J. Appl. Phys. 89 (2001) 7977–7982. https://doi.org/10.1063/1.1372661.

[73] V.Y. Davydov, I.N. Goncharuk, A.N. Smirnov, A.E. Nikolaev, W. V. Lundin, A.S. Usikov, A.A. Klochikhin, J. Aderhold, J. Graul, O. Semchinova, H. Harima, Composition dependence of optical phonon energies and Raman line broadening in hexagonal $Al_xGa_{1-x}N$ alloys, Phys. Rev. B. 65 (2002) 125203. https://doi.org/10.1103/PhysRevB.65.125203.

[74] V.Y. Davydov, Y.E. Kitaev, I.N. Goncharuk, A.N. Smirnov, J. Graul, O. Semchinova, D. Uffmann, M.B. Smirnov, A.P. Mirgorodsky, R.A. Evarestov, Phonon dispersion and Raman scattering in hexagonal GaN and AlN, Phys. Rev. B. 58 (1998) 12899–12907. https://doi.org/10.1103/PhysRevB.58.12899.

[75] J. Wang, C. Bayon, F. Demangeot, R. Pechou, A. Mlayah, A. Cros, B. Daudin, Raman spectroscopy of GaN and AlGaN nanowires: from ensemble to single nanowire study, in: J.-I. Chyi, Y. Nanishi, H. Morkoç, J. Piprek, E. Yoon, H. Fujioka (Eds.), Gall. Nitride Mater. Devices VIII, 2013: p. 86250P. https://doi.org/10.1117/12.2001564.

[76] S. Strite, GaN, AlN, and InN: A review, J. Vac. Sci. Technol. B Microelectron. Nanom. Struct. 10 (1992) 1237. https://doi.org/10.1116/1.585897.

[77] K. Lorenz, E. Nogales, S.M.C. Miranda, N. Franco, B. Méndez, E. Alves, G. Tourbot, B. Daudin, Enhanced red emission from praseodymium-doped GaN nanowires by defect engineering, Acta Mater. 61 (2013) 3278–3284. https://doi.org/10.1016/j.actamat.2013.02.016.

[78] M.W. Ullah, A. Kuronen, A. Stukowski, F. Djurabekova, K. Nordlund, Atomistic simulation of Er irradiation induced defects in GaN nanowires, J. Appl. Phys. 116 (2014) 124313. https://doi.org/10.1063/1.4896787.

[79] B.R. Judd, Optical Absorption Intensities of Rare-Earth Ions, Phys. Rev. 127 (1962) 750–761. https://doi.org/10.1103/PhysRev.127.750.

[80] G.S. Ofelt, Intensities of Crystal Spectra of Rare- Earth Ions, J. Chem. Phys. 37 (1962) 511–520. https://doi.org/10.1063/1.1701366.

[81] K. Binnemans, Interpretation of europium(III) spectra, Coord. Chem. Rev. 295 (2015) 1–45. https://doi.org/10.1016/j.ccr.2015.02.015.

[82] H.J. Lozykowski, W.M. Jadwisienczak, J. Han, I.G. Brown, Luminescence properties of GaN and $Al_{0.14}Ga_{0.86}N$/GaN superlattice doped with europium, Appl. Phys. Lett. 77 (2000) 767–769. https://doi.org/10.1063/1.1306645.

[83] H. Peng, C.-W. Lee, H.O. Everitt, C. Munasinghe, D.S. Lee, A.J. Steckl, Spectroscopic and energy transfer studies of Eu^{3+} centers in GaN, J. Appl. Phys. 102 (2007) 073520.

https://doi.org/10.1063/1.2783893.

[84] K.P. O'Donnell, P.R. Edwards, M. Yamaga, K. Lorenz, M.J. Kappers, M. Boćkowski, Crystalfield symmetries of luminescent Eu^{3+} centers in GaN: The importance of the $^5D_0$ to $^7F_1$ transition, Appl. Phys. Lett. 108 (2016) 022102. https://doi.org/10.1063/1.4939631.

[85] T. Koppe, H. Hofsäss, U. Vetter, Overview of band-edge and defect related luminescence in aluminum nitride, J. Lumin. 178 (2016) 267–281. https://doi.org/10.1016/j.jlumin.2016.05.055.

[86] A.M. Siladie, G. Jacopin, A. Cros, N. Garro, E. Robin, D. Caliste, P. Pochet, F. Donatini, J. Pernot, B. Daudin, Mg and in Codoped p-type AlN Nanowires for pn Junction Realization, Nano Lett. 19 (2019) 8357–8364. https://doi.org/10.1021/acs.nanolett.9b01394.

[87] G. Nogues, T. Auzelle, M. Den Hertog, B. Gayral, B. Daudin, Cathodoluminescence of stacking fault bound excitons for local probing of the exciton diffusion length in single GaN nanowires, Appl. Phys. Lett. 104 (2014). https://doi.org/10.1063/1.4868131.

[88] L. Bodiou, A. Oussif, A. Braud, J.-L. Doualan, R. Moncorgé, K. Lorenz, E. Alves, Effect of annealing temperature on luminescence in Eu implanted GaN, Opt. Mater. (Amst). 28 (2006) 780–784. https://doi.org/10.1016/j.optmat.2005.09.022.

[89] B. Mitchell, J. Poplawsky, D. Lee, A. Koizumi, Y. Fujiwara, V. Dierolf, The role of donor-acceptor pairs in the excitation of Eu-ions in GaN:Eu epitaxial layers, J. Appl. Phys. 115 (2014) 204501. https://doi.org/10.1063/1.4879253.

[90] S. Sanna, W.G. Schmidt, T. Frauenheim, U. Gerstmann, Rare-earth defect pairs in GaN: LDA+U calculations, Phys. Rev. B. 80 (2009) 104120. https://doi.org/10.1103/PhysRevB.80.104120.

[91] Y. Fujiwara, V. Dierolf, Present understanding of Eu luminescent centers in Eu-doped GaN grown by organometallic vapor phase epitaxy, Jpn. J. Appl. Phys. 53 (2014) 05FA13. https://doi.org/10.7567/JJAP.53.05FA13.

[92] K.H. Warnick, Y. Puzyrev, T. Roy, D.M. Fleetwood, R.D. Schrimpf, S.T. Pantelides, Room-temperature diffusive phenomena in semiconductors: The case of AlGaN, Phys. Rev. B. 84 (2011) 214109. https://doi.org/10.1103/PhysRevB.84.214109.

[93] H.J. Lozykowski, Kinetics of luminescence of isoelectronic rare-earth ions in III-V semiconductors, Phys. Rev. B. 48 (1993) 17758–17769. https://doi.org/10.1103/PhysRevB.48.17758.

[94] B. Mitchell, H. Austin, D. Timmerman, V. Dierolf, Y. Fujiwara, Temporally modulated energy shuffling in highly interconnected nanosystems, Nanophotonics. (2020) 1–26. https://doi.org/10.1515/nanoph-2020-0484.

[95] H.J. Lozykowski, W.M. Jadwisienczak, A. Bensaoula, O. Monteiro, Luminescence and excitation mechanism of Pr, Eu, Tb and Tm ions implanted into AlN, Microelectronics J. 36 (2005) 453–455. https://doi.org/10.1016/j.mejo.2005.02.045.

Fig. 1

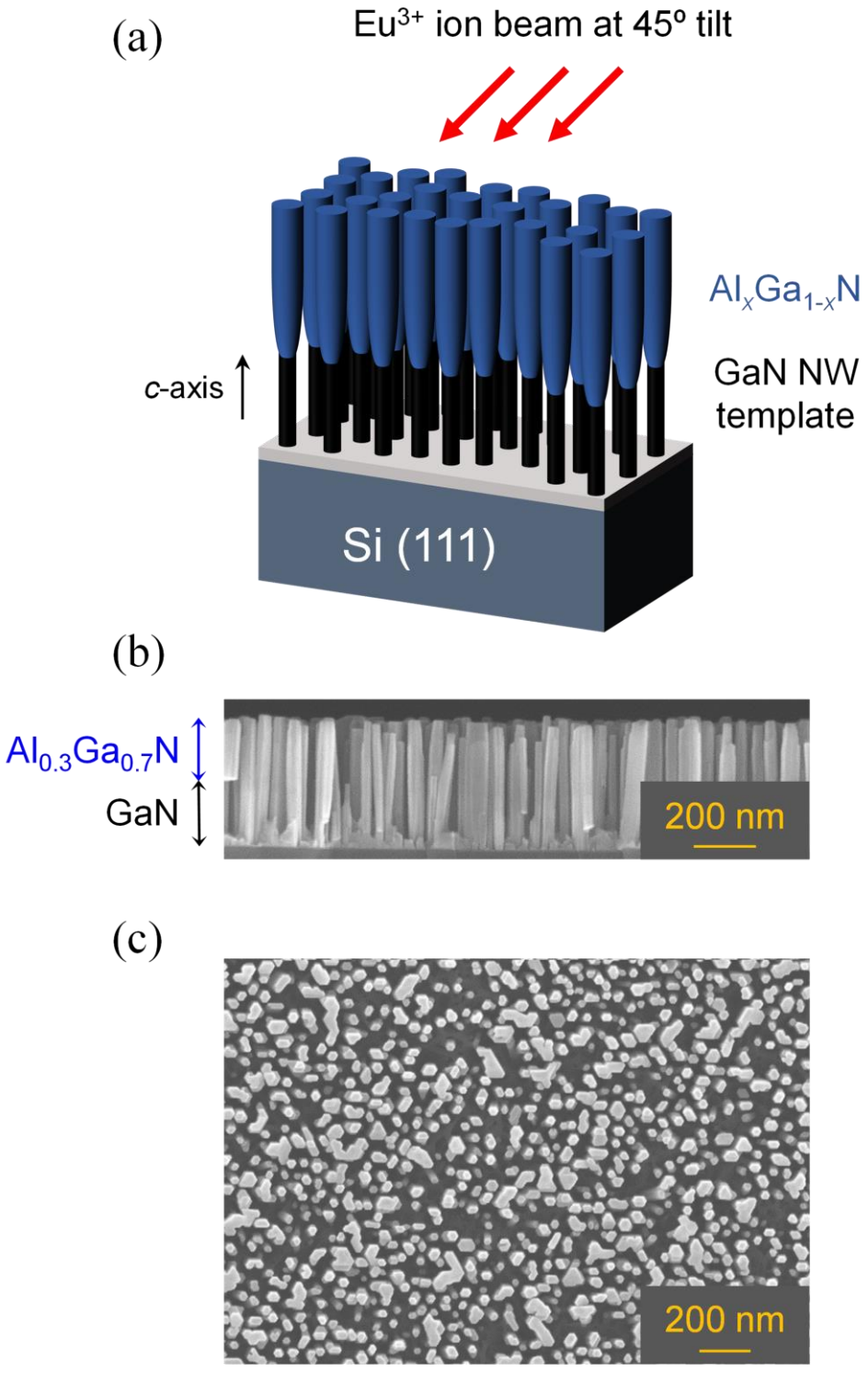
(a)
Eu3+ ion beam at 45° tilt
AlxGa1-xN
GaN NW template
c-axis
Si (111)
(b)
Al0.3Ga0.7N
GaN
200 nm
(c)
200 nm

Fig. 2

(a)

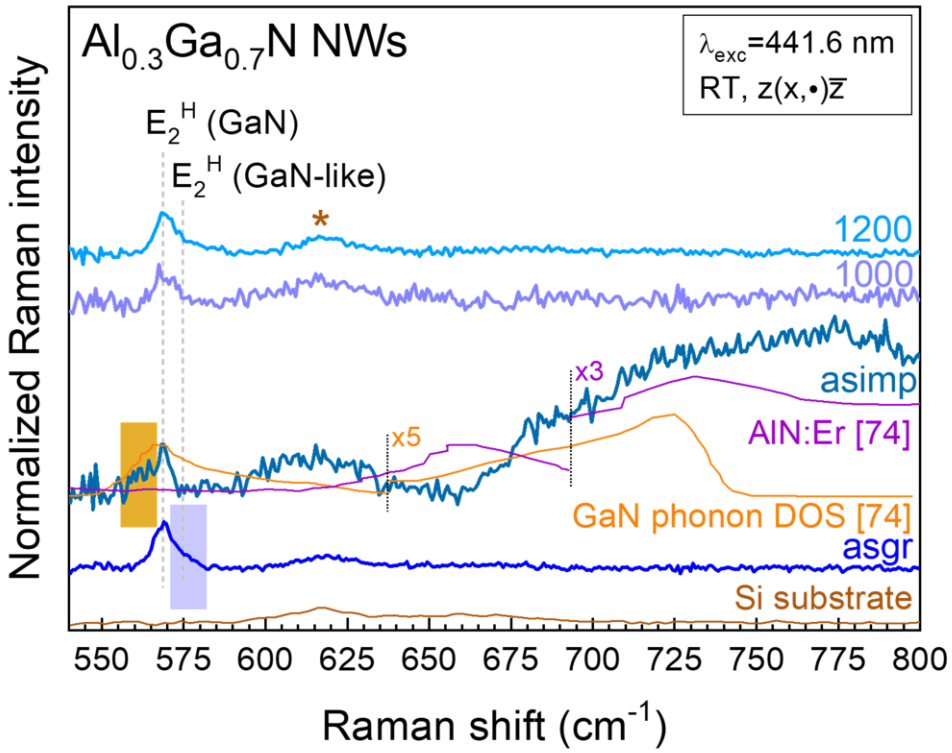
Al0.3Ga0.7N NWs
λexc=441.6 nm
RT, z(x,•)z̄
E2H (GaN)
E2H (GaN-like)
*
1200
1000
x3
asimp
x5
AlN:Er [74]
GaN phonon DOS [74]
asgr
Si substrate
Normalized Raman intensity
550 575 600 625 650 675 700 725 750 775 800
Raman shift (cm-1)

(b)

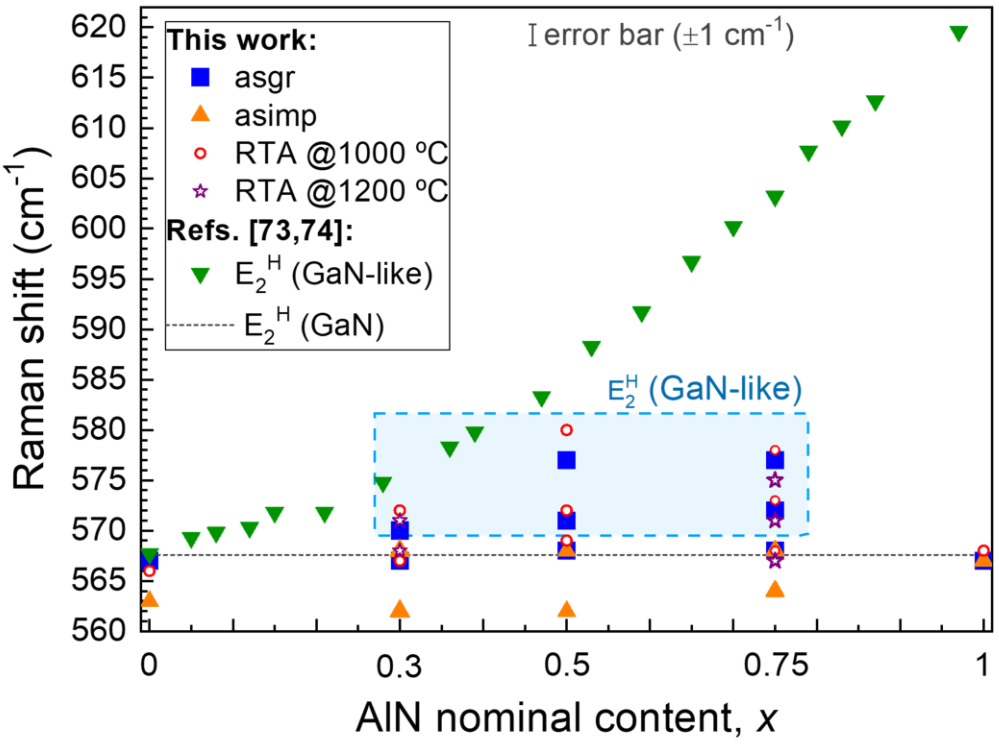
This work:
asgr
asimp
RTA @1000 ºC
RTA @1200 ºC
Refs. [73,74]:
E2H (GaN-like)
E2H (GaN)
error bar (±1 cm-1)
E2H (GaN-like)
Raman shift (cm-1)
620 615 610 605 600 595 590 585 580 575 570 565 560
0 0.3 0.5 0.75 1
AlN nominal content, x

Fig. 3

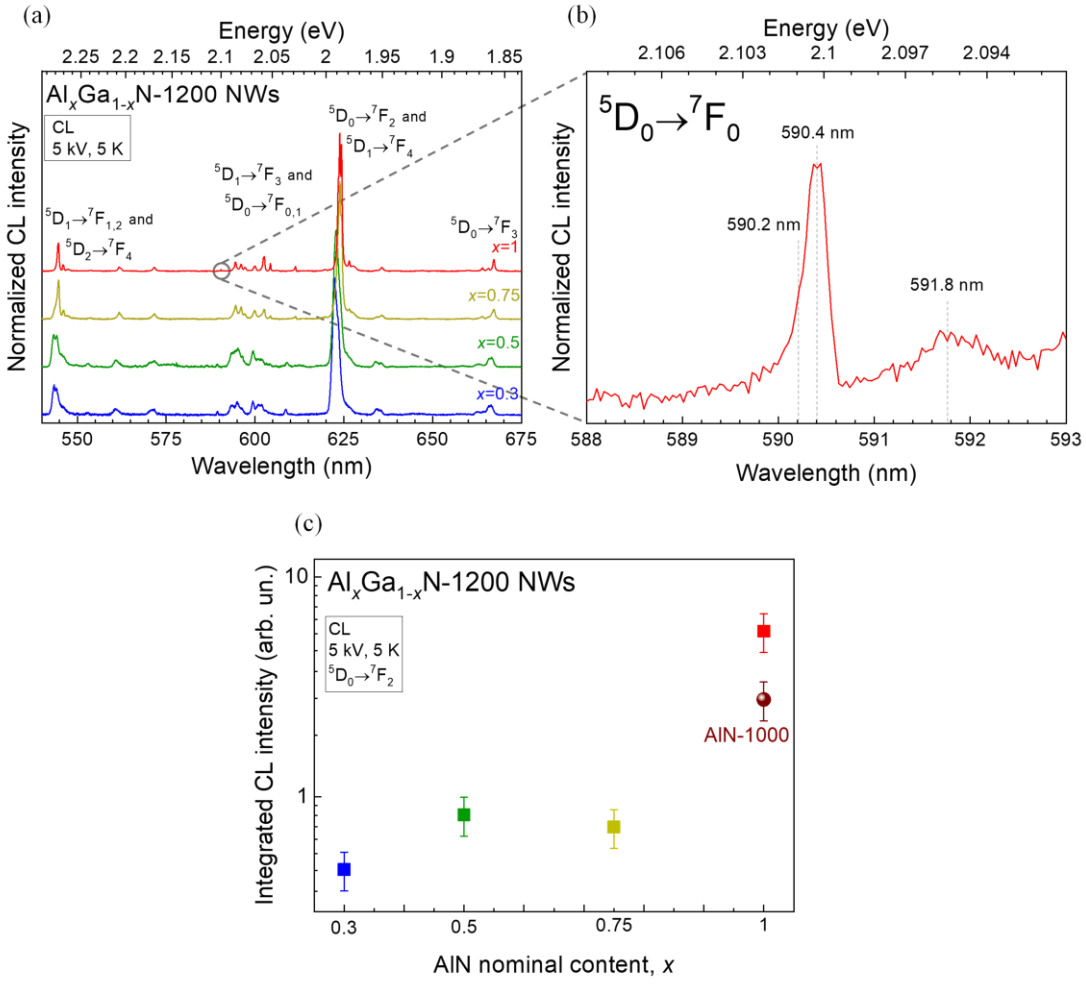
(a)
Energy (eV)
2.25 2.2 2.15 2.1 2.05 2 1.95 1.9 1.85
Al$_x$Ga$_{1-x}$N-1200 NWs
CL
5 kV, 5 K
$^5D_0 \rightarrow {}^7F_2$ and
$^5D_1 \rightarrow {}^7F_4$
$^5D_1 \rightarrow {}^7F_3$ and
$^5D_0 \rightarrow {}^7F_{0,1}$
$^5D_1 \rightarrow {}^7F_{1,2}$ and
$^5D_2 \rightarrow {}^7F_4$
$^5D_0 \rightarrow {}^7F_3$
x=1
x=0.75
x=0.5
x=0.3
Normalized CL intensity
550 575 600 625 650 675
Wavelength (nm)
(b)
Energy (eV)
2.106 2.103 2.1 2.097 2.094
$^5D_0 \rightarrow {}^7F_0$
590.4 nm
590.2 nm
591.8 nm
Normalized CL intensity
588 589 590 591 592 593
Wavelength (nm)
(c)
Al$_x$Ga$_{1-x}$N-1200 NWs
CL
5 kV, 5 K
$^5D_0 \rightarrow {}^7F_2$
AlN-1000
Integrated CL intensity (arb. un.)
10
1
0.3 0.5 0.75 1
AlN nominal content, x

Fig. 4

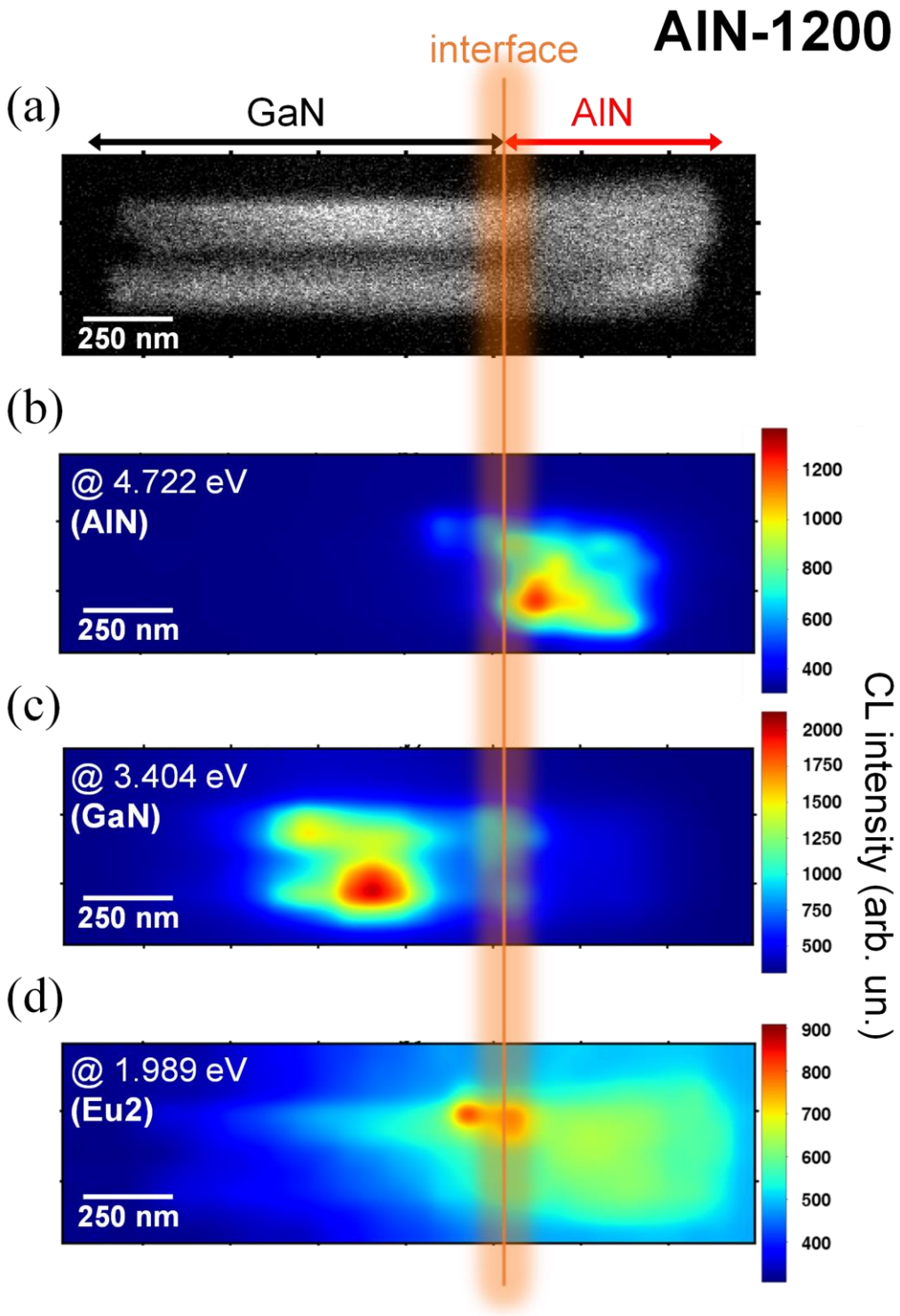
AlN-1200
interface
(a)
GaN
AlN
250 nm
(b)
@ 4.722 eV
(AlN)
250 nm
1200
1000
800
600
400
(c)
@ 3.404 eV
(GaN)
250 nm
2000
1750
1500
1250
1000
750
500
(d)
@ 1.989 eV
(Eu2)
250 nm
900
800
700
600
500
400
CL intensity (arb. un.)

Fig. 5

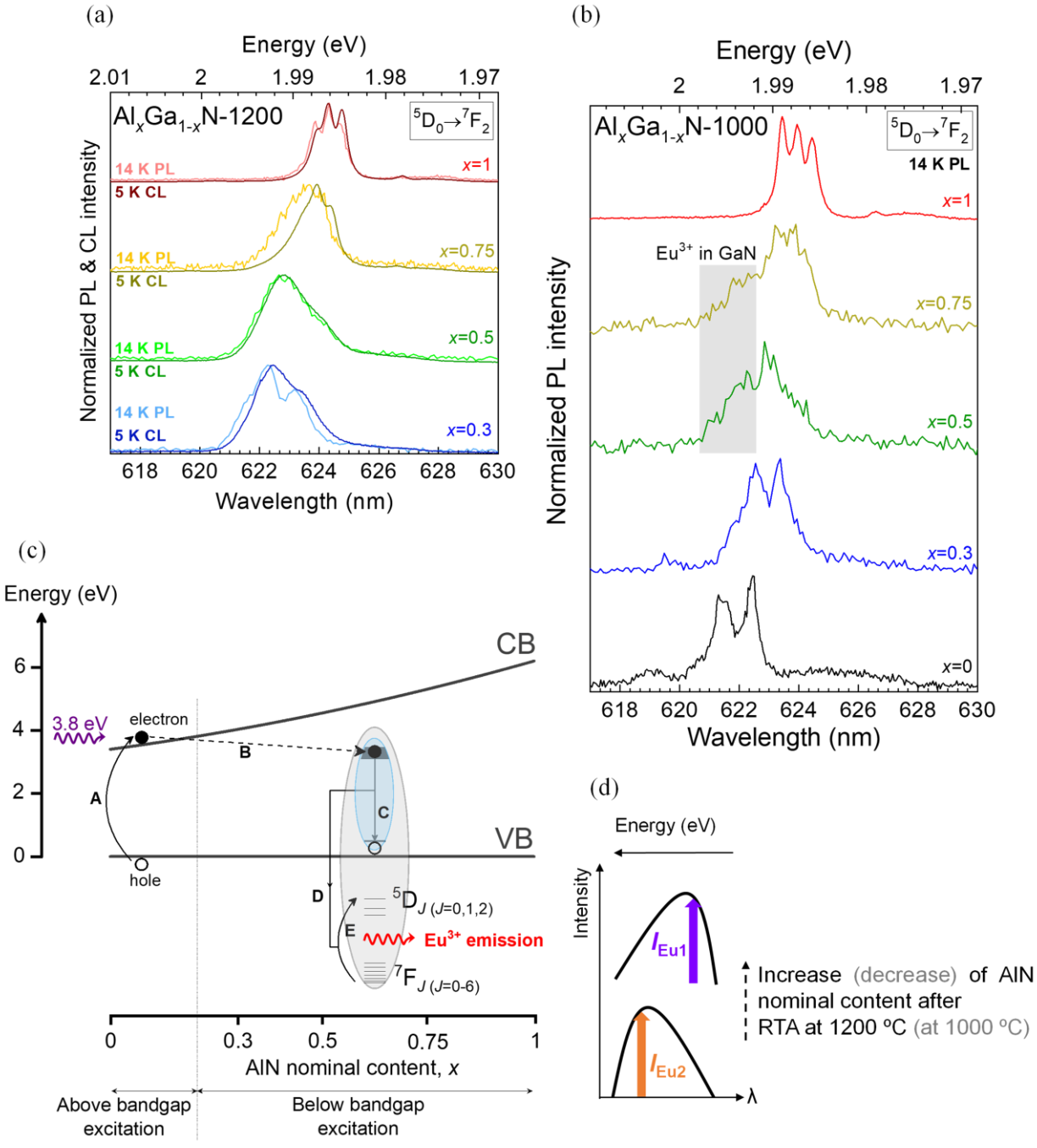
(a)
Energy (eV)
2.01
2
1.99
1.98
1.97
$Al_xGa_{1-x}N$-1200
$^5D_0 \rightarrow {}^7F_2$
14 K PL
5 K CL
x=1
x=0.75
x=0.5
x=0.3
Normalized PL & CL intensity
618
620
622
624
626
628
630
Wavelength (nm)
(b)
Energy (eV)
2
1.99
1.98
1.97
$Al_xGa_{1-x}N$-1000
$^5D_0 \rightarrow {}^7F_2$
14 K PL
x=1
Eu^{3+} in GaN
x=0.75
x=0.5
x=0.3
x=0
Normalized PL intensity
618
620
622
624
626
628
630
Wavelength (nm)
(c)
Energy (eV)
6
4
2
0
CB
VB
3.8 eV
electron
hole
A
B
C
D
E
^5D_J (J=0,1,2)
Eu^{3+} emission
^7F_J (J=0-6)
0
0.3
0.5
0.75
1
AlN nominal content, x
Above bandgap excitation
Below bandgap excitation
(d)
Energy (eV)
Intensity
I_{Eu1}
I_{Eu2}
λ
Increase (decrease) of AlN nominal content after RTA at 1200 ºC (at 1000 ºC)

Fig. 6

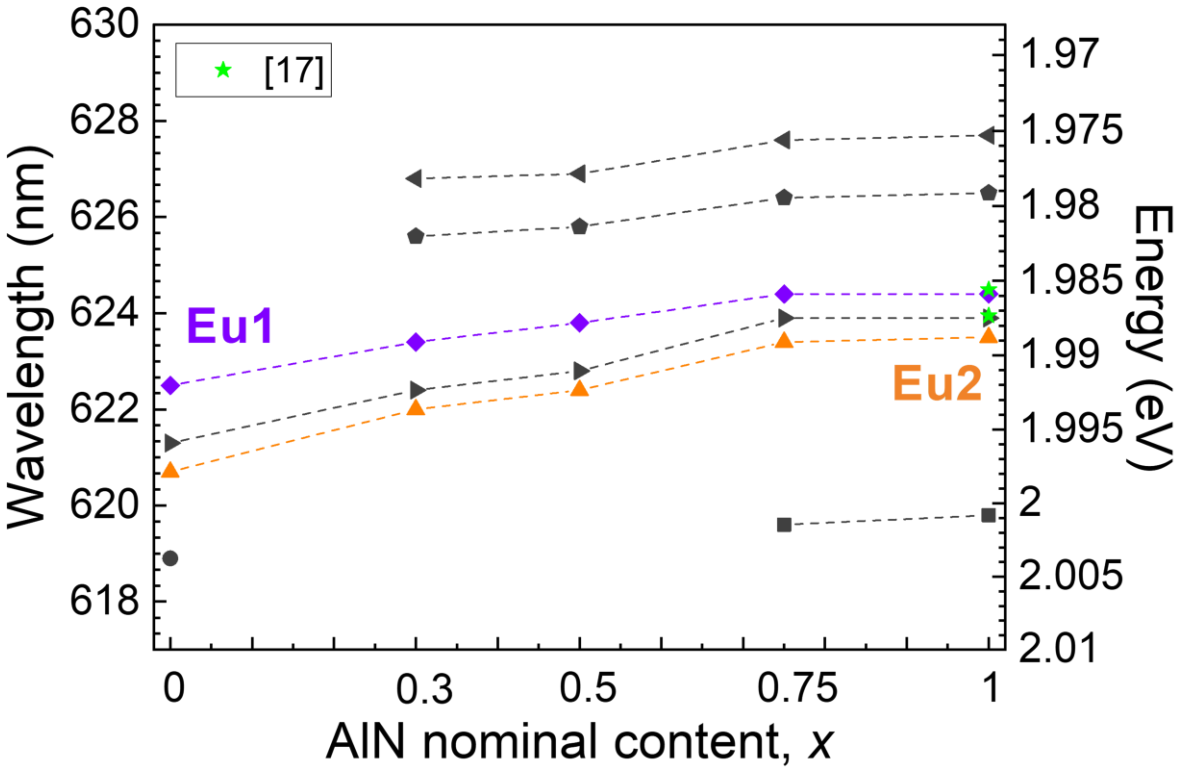
630
628
626
624
622
620
618
Wavelength (nm)
1.97
1.975
1.98
1.985
1.99
1.995
2
2.005
2.01
Energy (eV)
[17]
Eu1
Eu2
0
0.3
0.5
0.75
1
AlN nominal content, x

Fig. 7

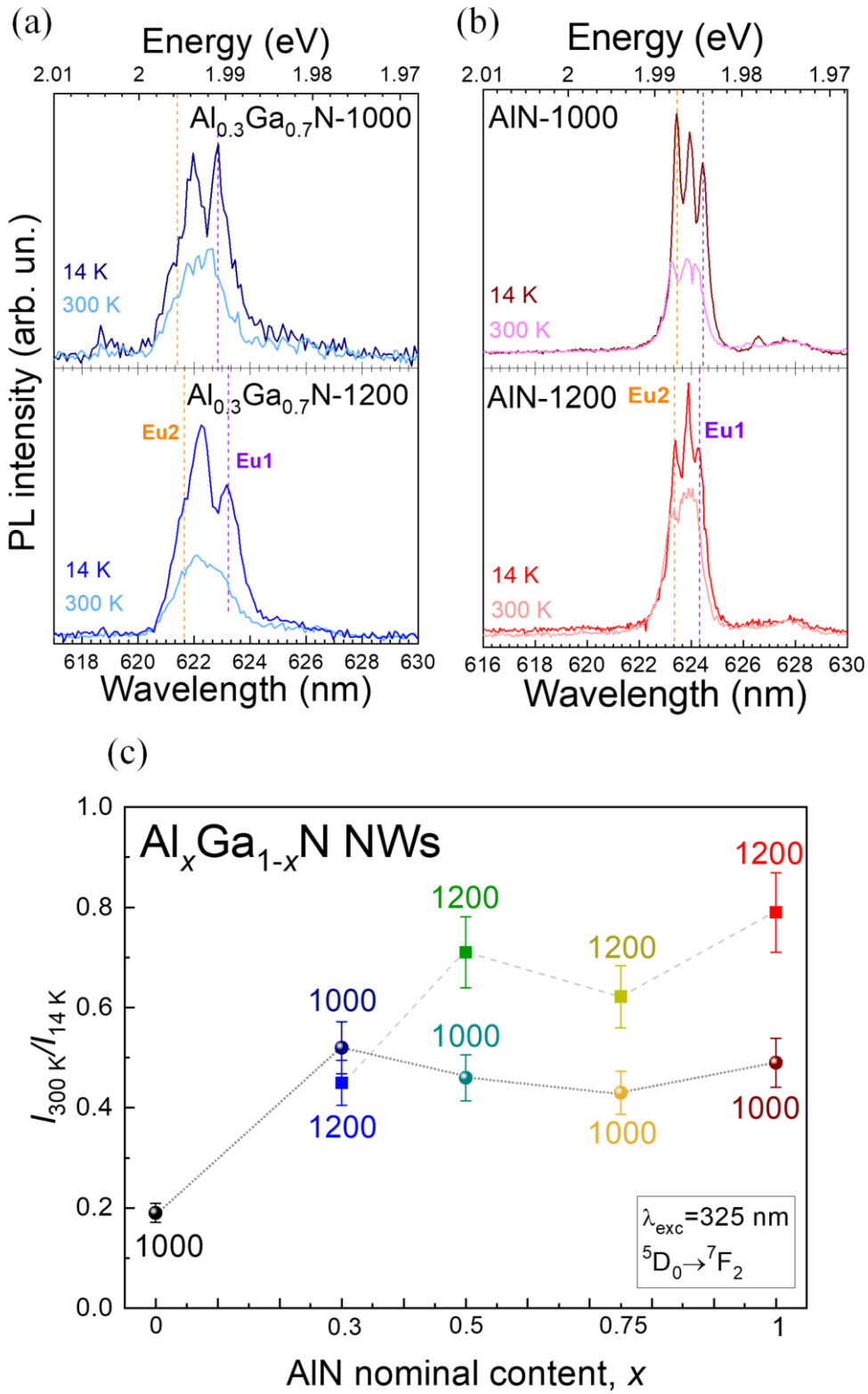
(a)
Energy (eV)
2.01
2
1.99
1.98
1.97
Al0.3Ga0.7N-1000
14 K
300 K
Al0.3Ga0.7N-1200
Eu2
Eu1
14 K
300 K
PL intensity (arb. un.)
618
620
622
624
626
628
630
Wavelength (nm)
(b)
Energy (eV)
2.01
2
1.99
1.98
1.97
AlN-1000
14 K
300 K
AlN-1200
Eu2
Eu1
14 K
300 K
616
618
620
622
624
626
628
630
Wavelength (nm)
(c)
AlxGa1-xN NWs
1.0
0.8
0.6
0.4
0.2
0.0
I300 K/I14 K
1200
1200
1200
1000
1000
1000
1200
1000
1000
λexc=325 nm
5D0→7F2
0
0.3
0.5
0.75
1
AlN nominal content, x

TOC

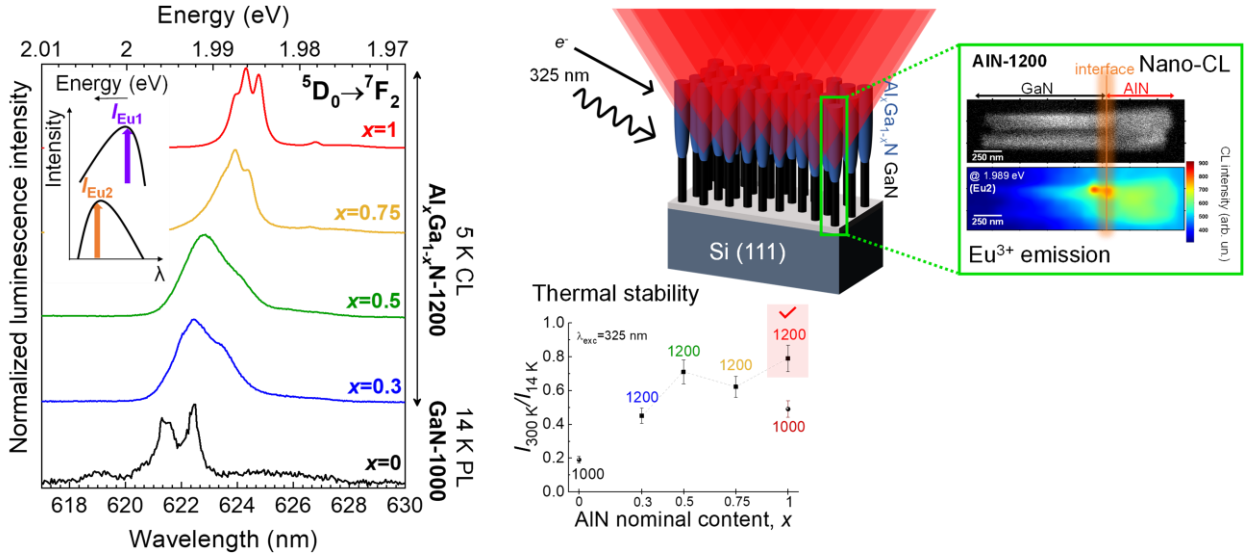
Energy (eV)
2.01
2
1.99
1.98
1.97
Normalized luminescence intensity
Energy (eV)
Intensity
I_{Eu1}
I_{Eu2}
λ
$^5D_0 \rightarrow {}^7F_2$
x=1
x=0.75
x=0.5
x=0.3
x=0
618
620
622
624
626
628
630
Wavelength (nm)
$Al_xGa_{1-x}N$-1200
5 K CL
GaN-1000
14 K PL
e⁻
325 nm
$Al_xGa_{1-x}N$ GaN
Si (111)
AlN-1200
interface
Nano-CL
GaN
AlN
250 nm
@ 1.989 eV
(Eu2)
CL intensity (arb. un.)
Eu^{3+} emission
Thermal stability
λ_{exc}=325 nm
$I_{300\ K}/I_{14\ K}$
1.0
0.8
0.6
0.4
0.2
0.0
1200
1200
1200
1000
1000
0
0.3
0.5
0.75
1
AlN nominal content, x

Supplementary Information:

Eu^{3+} optical activation engineering in $Al_xGa_{1-x}N$ nanowires for red solid-state nano-emitters

J. Cardoso,[,†] G. Jacopin,[⊥] D. Nd. Faye,[‡,□], A. M. Siladie,[ǀ] B. Daudin,[ǀ] E. Alves,[‡] K. Lorenz,[‡,□] T. Monteiro,[†] M. R. Correia[†] and N. Ben Sedrine[*,†]*

[†]Departamento de Física e I3N, Universidade de Aveiro, Campus Universitário de Santiago, 3810-193 Aveiro, Portugal
[⊥] Univ. Grenoble Alpes, CNRS, Grenoble INP, Institut Néel, 38000 Grenoble, France
[‡]IPFN, Instituto Superior Técnico, Campus Tecnológico e Nuclear, Estrada Nacional 10, P-2695-066 Bobadela LRS, Portugal
[ǀ]Univ. Grenoble Alpes, CEA/CNRS Group, "Nanophysique et Semiconducteurs", F-38000 Grenoble, France
[□]Instituto de Engenharia de Sistemas de Computadores – Microsystems and Nanotechnology (INESC-MN), Rua Alves Redol, 1000-029 Lisboa, Portugal

S1. SCANNING ELECTRON MICROSCOPY (SEM)

Representative SEM images of the $Al_xGa_{1-x}N$ as-grown ($Al_xGa_{1-x}N$-asgr) nanowires (NWs) are exhibited in Fig. S1 for x = 0 (*a*, *b*); x = 0.5 (*c*, *d*); x = 0.75 (*e*, *f*); and x = 1 (*g*, *h*).

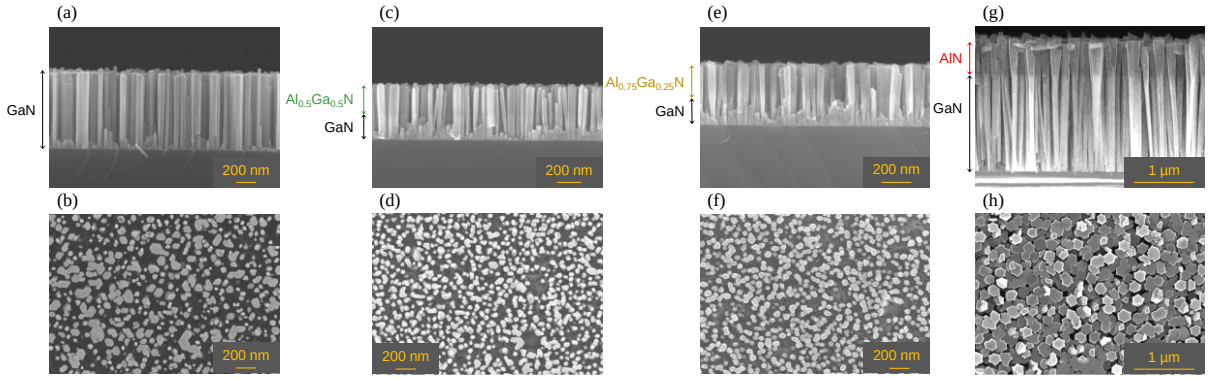

Fig. S1: Representative SEM images of the GaN-asgr (*a*, *b*), $Al_{0.5}Ga_{0.5}N$-asgr (*c*, *d*), $Al_{0.75}Ga_{0.25}N$-asgr (*e*, *f*), and AlN-asgr (*g*, *h*) NWs in side-view and top-view, respectively. Vertical side arrows correspond to the different NW segments.

S2. µ-RAMAN

S2.1. µ-Raman response of the $Al_xGa_{1-x}N$ NWs

Fig. S2 depicts the µ-Raman spectra of the NWs (*a*) $Al_xGa_{1-x}N$-asgr, (*b*) as-implanted ($Al_xGa_{1-x}N$-asimp), (*c*) after rapid thermal annealing (RTA) at 1000 ℃ ($Al_xGa_{1-x}N$-1000), and (*d*) after RTA at

1200 ℃ ($Al_xGa_{1-x}N$-1200). The calculated phonon density of states (DOS) for GaN and the disorder-induced Raman spectrum of AlN layers implanted with erbium (Er) are included in (b) for comparison [1]. The μ-Raman response of the Si (111) substrate is shown in Fig. S2*a*. The signal detected between ~600-700 cm^{-1} is related to Si native oxide, SiO_2 [2].

Second-order Raman scattering processes are activated after Eu^{3+}-implantation and are characterized by the detection of an unstructured broadband (dashed shape in Fig. S2*b*). Such broadband, closely associated with the GaN (AlN) phonon DOS in GaN (AlN) NWs, is seen to shift to higher frequencies from GaN to AlN. This important observation corroborates the results that have confirmed the $Al_xGa_{1-x}N$ top-section as the most affected by Eu^{3+}-implantation.

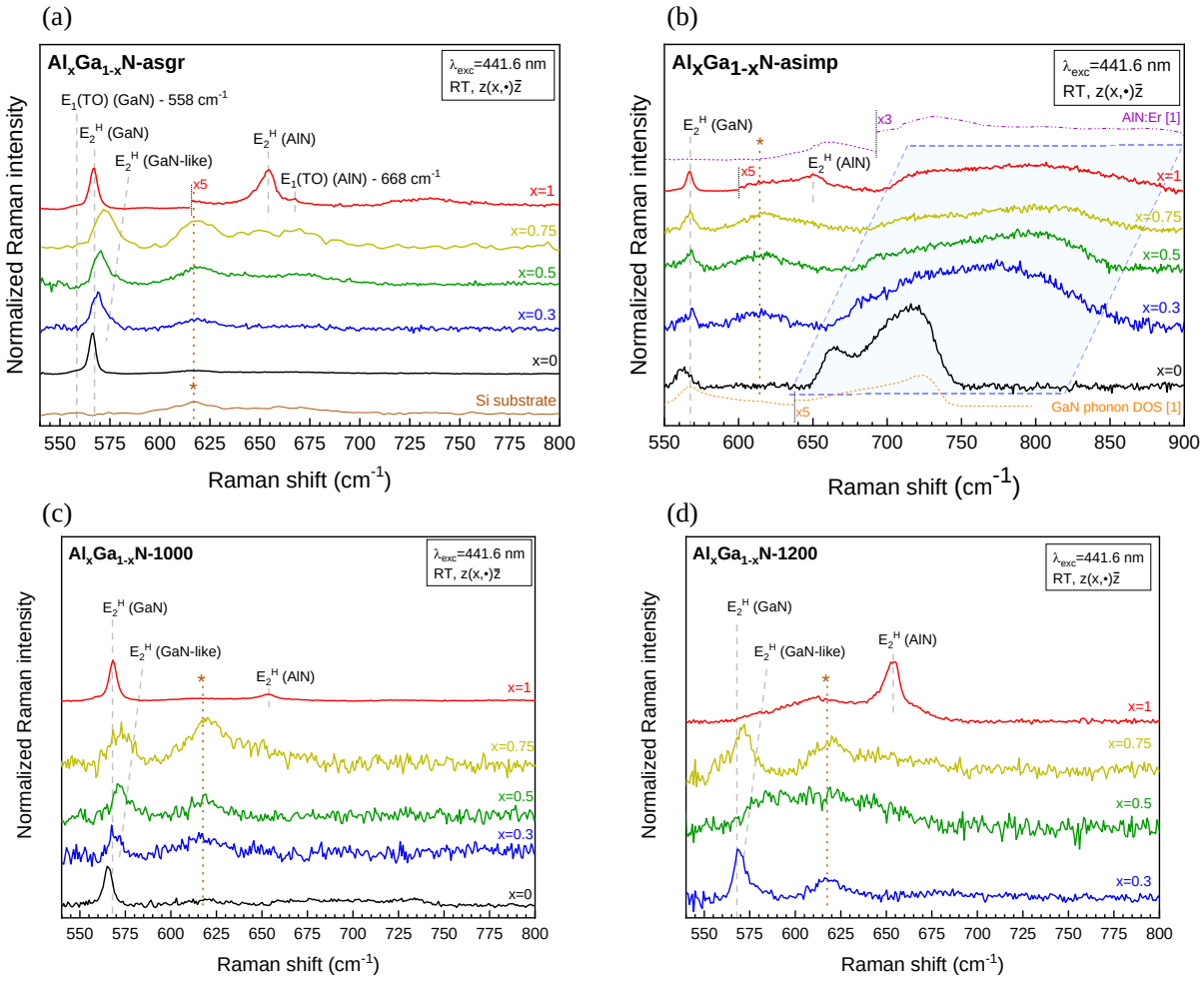

Fig. S2: RT normalized μ-Raman spectra of the (*a*) $Al_xGa_{1-x}N$-asgr, (*b*) $Al_xGa_{1-x}N$-asimp, (*c*) $Al_xGa_{1-x}N$-1000, and (*d*) $Al_xGa_{1-x}N$-1200 NW ensemble, for all samples, using laser excitation of 441.6 nm. The spectra were normalized to the maximum of the E_2^H (GaN) phonon intensity. In (*d*), the spectrum of the AlN-1200 NWs was normalized to the maximum of the E_2^H (AlN) phonon intensity. The feature arising from the Si (111) substrate is indicated by (*). The calculated phonon DOS for GaN and the disorder-induced Raman spectrum for Er-implanted AlN layers are included in (*b*) for comparison [1].

The E_2^H (GaN) phonon is not detected for $Al_{0.5}Ga_{0.5}N$-1200 and AlN-1200 NWs. For the AlN-1200 NWs, the reduction/absence of this phonon may be due to an increase in the optical absorption along the NW structure caused by the generated optical defects after RTA at 1200 ℃, since the

morphology and structure of the NWs are not altered by Eu^{3+}-implantation and RTA [3]. For the $Al_{0.5}Ga_{0.5}N$-1200 NWs, a similar effect might be occurring since the detection of the E_2^H (GaN) was not possible (even by probing distinct regions of the sample).

S2.2. Deconvolution of E_2^H (GaN) and E_2^H (GaN-like) phonons

The deconvolution method consists of the decomposition into the minimum number of Lorentzian components necessary to best describe the μ-Raman response in the E_2^H (GaN) region. For $Al_xGa_{1-x}N$-asgr NWs (x = 0.3, 0.5, and 0.75), the asymmetry of the E_2^H indicates the existence of distinct contributions: i) E_2^H (GaN), and ii) E_2^H (GaN-like) phonons at higher frequencies. In the deconvolution procedure, the first component was fixed (frequency, ω, and full width at half maximum, FWHM) to the values determined for the E_2^H (GaN) of GaN-asgr and AlN-asgr (ω between 567-569 cm^{-1}, and FWHM between 3-5 cm^{-1}). The second contribution [E_2^H (GaN-like)] can have more than one Lorentzian component (one, for x = 0.3; and two, for x = 0.5 and x = 0.75) which parameters were varied until the fit converged. The same procedure was performed for $Al_xGa_{1-x}N$-1000 and $Al_xGa_{1-x}N$-1200 NWs.

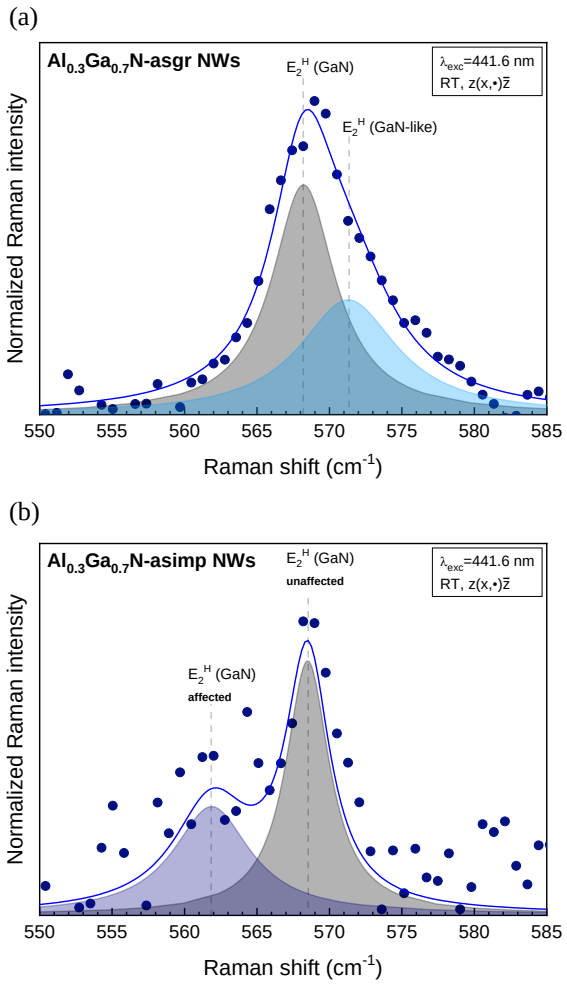

Fig. S3: Results of the deconvolution of the E_2^H (GaN) phonon response by using two Lorentzian functions for (*a*) $Al_{0.3}Ga_{0.7}N$-asgr, and (*b*) $Al_{0.3}Ga_{0.7}N$-asimp NWs.

For the $Al_xGa_{1-x}N$-asimp, the procedure was slightly different since the asymmetry of the E_2^H phonon become visible at lower frequencies. In this case, two contributions were deconvoluted: i) E_2^H (GaN) from a region of the GaN NW template unaffected by Eu^{3+}-implantation, and ii) E_2^H (GaN) from the GaN NW template region affected by Eu^{3+}-implantation.

The deconvolution procedures are highlighted in Fig. S3 for (*a*) $Al_{0.3}Ga_{0.7}N$-asgr, and (*b*) $Al_{0.3}Ga_{0.7}N$-asimp NWs. Table S1 summarizes the results for E_2^H phonon frequencies and FWHM obtained for all the samples. It is noteworthy to mention that the error of the deconvolution procedure is higher for the as-implanted samples due to the reduced intensity and signal-to-noise ratio of the E_2^H response.

Table S1: Summary of the parameters extracted from the deconvolution (frequency, ω, and FWHM, in cm^{-1}) of the E_2^H response. Deconvoluted peaks related to both the GaN NW template (black), and the $Al_xGa_{1-x}N$ top-section (blue) are indicated. (N/A: not applicable).

$Al_xGa_{1-x}N$	as grown	as implanted	RTA at 1000 ℃	RTA at 1200 ℃
***x* = 0**	ω = 567±1 (FWHM = 4±1)	563±1 (9±1)	566±1 (5±1)	N/A
***x* = 0.3**	568±1 (5±1)	568±1 (4±1)	567±1 (4±1)	568±1 (4±1)
	571±1 (8±2)	562±1 (6±3)	572±1 (5±2)	571±1 (5±2)
***x* = 0.5**	568±1 (4±1)	568±1 (5±1)	569±3 (5±5)	N/A
	571±1 (6±1)	562±2 (10±4)	572±2 (7±4)	
	577±2 (7±7)		580±2 (10±4)	
***x* = 0.75**	568±2 (4±1)	568±1 (5±1)	568±1 (5±2)	567±2 (5±7)
	572±2 (7±7)	564±1 (3±2)	573±1 (5±3)	571±2 (8±8)
	577±5 (7±7)		578±1 (6±2)	575±2 (5±8)
***x* = 1**	567±1 (5±1)	567±1 (5±1)	568±1 (5±1)	N/A

S2.3. Determination of hydrostatic strain in GaN and AlN NWs

The frequency shift ($\Delta\omega = \omega - \omega_0$) of the E_2^H phonon (ω) relatively to that of the as-grown NWs (ω_0) can be used to estimate the stress induced by Eu^{3+}-implantation and its evolution after RTA. Assuming that RE-implantation introduces hydrostatic stress ($\sigma_{xx} \approx \sigma_{yy} \approx \sigma_{zz}$) in the crystalline

lattice [4–6], stress can be expressed in terms of the frequency shift through the following expression [7]:

$$\sigma_{xx} = \frac{\Delta\omega}{2\tilde{a}_\lambda + \tilde{b}_\lambda}. \qquad \text{(eq. S1)}$$

The parameters $\tilde{a}_\lambda$ and $\tilde{b}_\lambda$ correspond to the phonon deformation potentials and their values are respectively -1.20 cm^{-1}/GPa (-1.28 cm^{-1}/GPa) and -1.12 cm^{-1}/GPa (-1.65 cm^{-1}/GPa) for GaN (AlN), according to Wagner *et al*. [7]. It is important to refer that for GaN NWs, the frequency shift of the E_2^H (GaN) was considered, while for AlN NWs, the shift of the E_2^H (AlN) phonon was used. In our calculations, the error of the phonon deformation potentials was estimated to be 20% based on the dispersion of the data presented on reference [7]. When $\sigma_{xx} > 0$, the stress is tensile, while $\sigma_{xx} < 0$ corresponds to a compressive stress. Fig. S4 depicts the evolution of the σ_{xx} with the distinct treatments applied to GaN and AlN NWs.

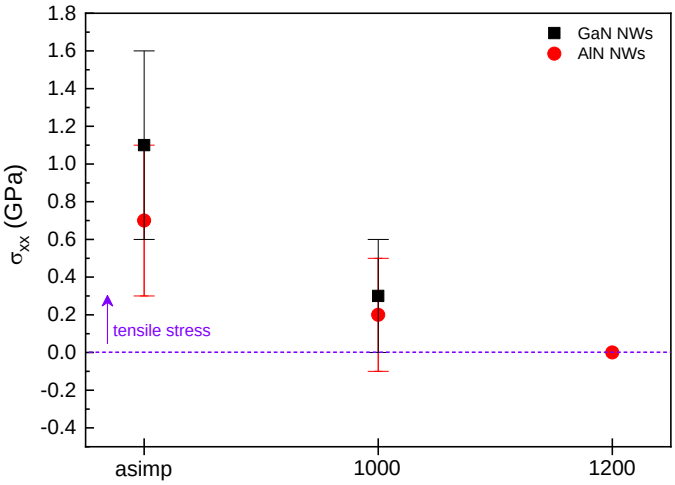

Fig. S4: Hydrostatic stress (σ_{xx}) evolution in GaN and AlN NWs with Eu^{3+}-implantation and RTA at 1000 ℃ and 1200 ℃. The dashed line represents the strained-free situation (for as-grown NWs). $\sigma_{xx} > 0$ corresponds to tensile stress.

S3. CATHODOLUMINESCENCE (CL) AND PHOTOLUMINESCENCE (PL)

S3.1. CL response of the $Al_xGa_{1-x}N$ NWs

Fig. S5 depicts a magnification of the 5 K CL spectra of the $Al_xGa_{1-x}N$-1200 NW ensemble around distinct Eu^{3+} transitions: (*a*) $^5D_2 \rightarrow {}^7F_{0,1,2,3}$ and $^5D_1 \rightarrow {}^7F_0$, (*b*) $^5D_1 \rightarrow {}^7F_{1,2}$ and $^5D_2 \rightarrow {}^7F_4$; (*c*) $^5D_0 \rightarrow {}^7F_{0,1}$ and $^5D_1 \rightarrow {}^7F_3$; (*d*) $^5D_0 \rightarrow {}^7F_2$ and $^5D_1 \rightarrow {}^7F_4$; (*e*) $^5D_0 \rightarrow {}^7F_3$, and (*f*) $^5D_0 \rightarrow {}^7F_4$.

The position of the emission lines (obtained from 5 K CL spectra) and their assignment to the respective transition are listed in Table S2. For GaN-1000 NWs, the values were extracted from the 14 K high-resolution (HR) PL spectrum. Table S2 also includes 11 K CL results from *in situ* Eu^{3+}-doped single crystal AlN [8]. The $^5D_0 \rightarrow {}^7F_2$ and $^5D_1 \rightarrow {}^7F_4$ transitions lie in the same energy range [8], and therefore the assignment of these transitions can be complex. For AlN NWs, the assignment to the $^5D_0 \rightarrow {}^7F_2$ transition was made based on PL results obtained under 325 nm laser excitation. Since no other emissions from the excited state $^5D_1$ were detected in PL experiments, we can exclude its contribution and thus make the respective assignment. For $Al_xGa_{1-x}N$ NWs

(x = 0.3, 0.5, and 0.75), the assignment was done based on the peaks' shift from those recorded for AlN NWs as well as by their intensity.

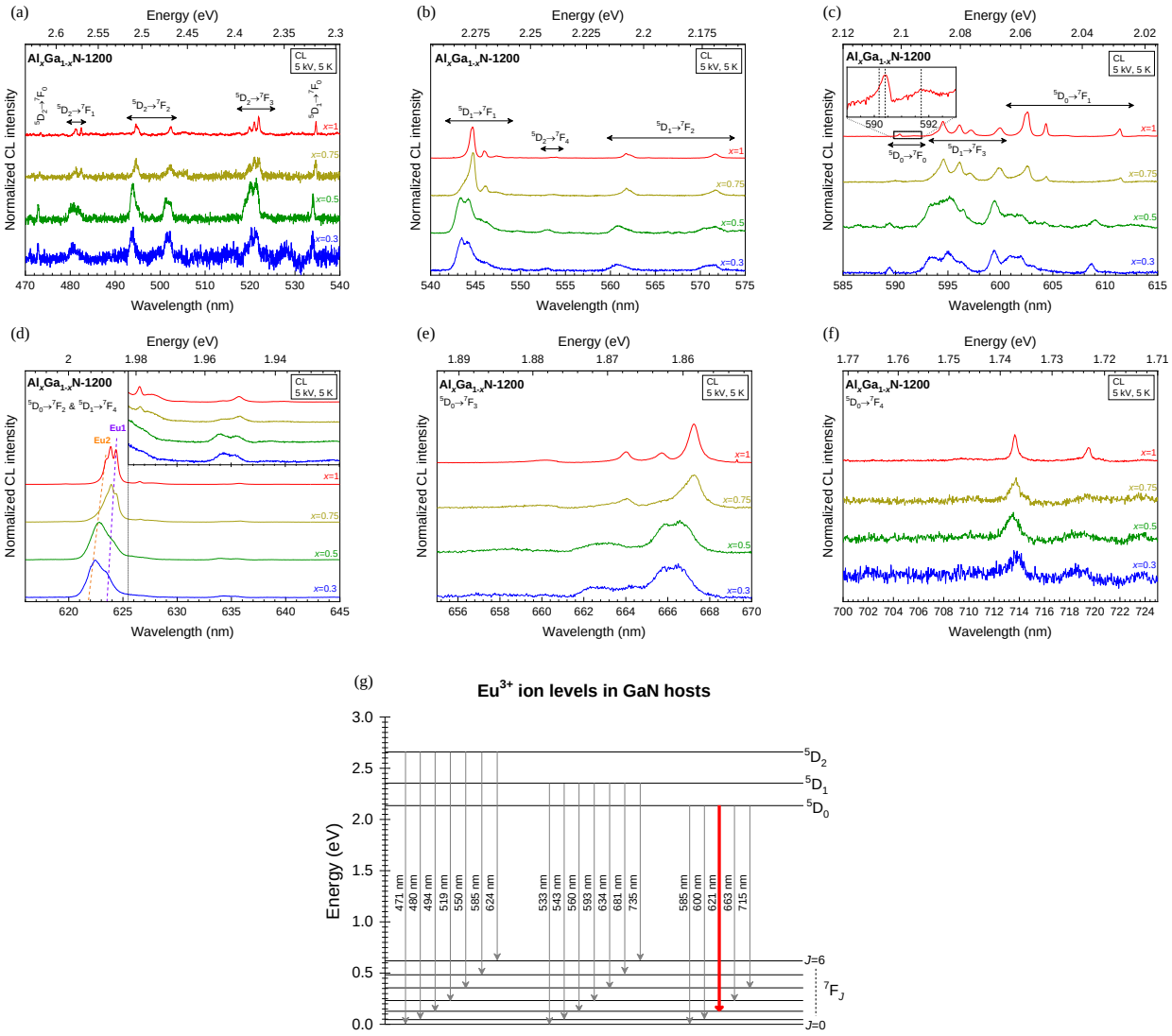

Fig. S5: 5 K CL spectra of the $Al_xGa_{1-x}N$-1200 NW ensemble around distinct Eu^{3+} transitions: (*a*) $^5D_2 \rightarrow {}^7F_{0,1,2,3}$ and $^5D_1 \rightarrow {}^7F_0$; (*b*) $^5D_1 \rightarrow {}^7F_{1,2}$ and $^5D_2 \rightarrow {}^7F_4$; (*c*) $^5D_0 \rightarrow {}^7F_{0,1}$ and $^5D_1 \rightarrow {}^7F_3$; (*d*) $^5D_0 \rightarrow {}^7F_2$ and $^5D_1 \rightarrow {}^7F_4$; (*e*) $^5D_0 \rightarrow {}^7F_3$; and (*f*) $^5D_0 \rightarrow {}^7F_4$. In (*c*), the inset shows a magnification around the $^5D_0 \rightarrow {}^7F_0$ transition for the AlN-1200 NWs. In (*d*), the inset corresponds to a magnification of the emission around 625 and 645 nm. Dashed lines in (*d*) represent the transitions identified as Eu1 (violet) and Eu2 (orange) centers. (*g*) Schematic of the Eu^{3+} ion energetic levels in GaN hosts [9,10]. The most intense transition ($^5D_0 \rightarrow {}^7F_2$) is represented by a red arrow.

Table S2: Peak assignment of the Eu^{3+} intra-$4f^6$ transitions observed in 5 K CL spectra of the $Al_xGa_{1-x}N$-1200 samples. For the sample GaN-1000, the peaks were extracted from the 14 K HR-PL spectrum. The values obtained by Gruber *et al*. for Eu^{3+}-doped *w*-AlN single crystal are included for comparison [8]. (wk: weak or low intensity; *: shoulder).

Transition (nm) & Assignment	**GaN-1000** PL 14 K (±0.1 nm)	**$Al_{0.3}Ga_{0.7}N$-1200** CL 5 K (±0.1 nm)	**$Al_{0.5}Ga_{0.5}N$-1200** CL 5 K (±0.1 nm)	**$Al_{0.75}Ga_{0.25}N$-1200** CL 5 K (±0.1 nm)	**AlN-1200** CL 5 K (±0.1 nm)	**Eu^{3+}-doped *w*-AlN single crystal** CL 11 K Gruber *et al*. [8]
$^5D_2 \rightarrow {}^7F_0$		472.8	472.9	473.3	471.8 (wk) 473.5	
$^5D_2 \rightarrow {}^7F_1$		480.6	480.7 481.8	481.3 482.4	481.3 482.4	
$^5D_2 \rightarrow {}^7F_2$		493.8 501.3 502.1	493.9 494.9* 501.4 502.2	494.7 495.1* 501.8* 502.4	494.6 494.9 495.2* 502.4	
$^5D_2 \rightarrow {}^7F_3$		519.1 (wk) 520.3 521.3	519.0 520.2 521.3	5199 520.9 522.0	517.6 (wk) 519.9 520.9 521.9	
$^5D_1 \rightarrow {}^7F_0$		534.0	534.1	534.6	534.5* 534.7	534.67 534.90
$^5D_1 \rightarrow {}^7F_1$		543.4 544.0 545.6	543.4 544.2 545.4 546.3	543.8* 544.7 546.1 547.4	544.4* 544.7 546.0 546.2* 547.3 547.7* 549.0 549.9	544.63* 544.87 546.16 546.38
$^5D_2 \rightarrow {}^7F_4$		552.8 (wk)	553.1	553.3 553.9	553.4 554.0	
$^5D_1 \rightarrow {}^7F_2$		560.7 570.6 571.5	560.8 570.5 571.6	561.8 562.2* 570.8* 571.7	561.8 562.2 564.2 571.7	562.01* 562.18 562.52* 563.80* 571.80* 571.91
$^5D_0 \rightarrow {}^7F_0$		589.4 (wk)	589.4	590.0 (wk) 591.8 (wk)	590.2* 590.4 591.8	590.34
$^5D_1 \rightarrow {}^7F_3$		593.4	593.6	593.8*	593.9*	593.50* 593.80

				594.5	594.5	594.52 594.74* 595.80*
		595.0	595.2	596.1	596.1	596.08
		596.3*	596.5	597.1	597.2	597.15* 597.32
		599.4	599.5	599.9	600.0	599.60* 599.92
$^5D_0 \rightarrow {}^7F_1$	601.2 607.5	600.9 601.9 603.0 608.7	600.9 602.0 603.3 (wk) 609.0	601.8* 602.5 604.4 611.4	601.9* 602.6 604.4 606.1 610.9* 611.4 613.2 614.1 615.2	 602.49 604.35
$^5D_0 \rightarrow {}^7F_2$ and/or $^5D_1 \rightarrow {}^7F_4$	 618.9 620.7 621.3 622.5	 622.0* 622.4 623.4 625.6* 626.8* 634.1 635.3	 622.4* 622.8 623.8 625.8* 626.9* 634.0 635.5	619.6 623.4* 623.9 624.4 626.4 627.6* 634.3 635.7	619.7 623.5 (Eu2) 623.9 624.4 (Eu1) 626.5 627.3* 627.7 630.5 634.0* 634.3 635.7 638.9 639.8	620.34* 620.68 623.95 624.49 626.66 627.00* 629.00 634.31* 635.79 637.14 639.00
$^5D_0 \rightarrow {}^7F_3$	661.6 663.1 663.9 665.2	662.3 663.1* 664.3 665.8 666.5	662.6 663.4* 664.5 665.9 666.6	647.1 (wk) 660.1 662.9* 664.0 665.6* 667.2	646.3* 647.2 648.0 660.2 663.1* 664.0 665.7 667.3	 664.03 665.74 667.33
$^5D_0 \rightarrow {}^7F_4$						707.21

		713.4 (wk)	713.5	713.6	709.4 (wk) 713.7 719.5	709.77 713.84 719.71

The near band edge (NBE) emission of $Al_xGa_{1-x}N$ alloys follows the behavior of the bandgap energy, E_g, as a function of the AlN content, x, although it occurs at slightly lower energies (~ tens of meV – exciton binding energy [11]). The bandgap energy of $Al_xGa_{1-x}N$ alloys follows the empirical Vegard's rule, $E_g(Al_xGa_{1-x}N) = (1-x)E_g(GaN) + xE_g(AlN) + bx(1-x)$, with b the bowing parameter (recommended value is 1 eV [12]).

Fig. S6*a* depicts the 5 K CL spectra of the $Al_xGa_{1-x}N$-asgr NWs ($x > 0$) obtained when the electron beam is focused on the NW ensemble and single NW (spot mode) in the spectral range of the NBE emission. For low AlN nominal contents ($x = 0.3$, and 0.5), the CL response reveals two and three peaks, respectively, at energies below the expected values for the NBE emission. This is in agreement with the μ-Raman results, corroborating the hypothesis that: i) compositional fluctuations exist in the NWs, and ii) lower AlN content than the nominal value and/or a tensile strain in the $Al_xGa_{1-x}N$ top-section grown on top of GaN NW template might be involved. For the high AlN nominal content NWs ($x = 0.75$, and 1), the emission is broader, occurs for energies lower than those expected for the NBE, and does not follow the trend of the bandgap energy. Although for $x = 0.75$, the existence of compositional fluctuations is a possibility, this is not valid for $x = 1$ (since there is no Ga flux). This emission might be assigned to donor-acceptor pair (DAP) transitions involving AlN-related defects, as nitrogen vacancies [13,14]. Moreover, in spot mode, it is possible to observe that the emission consists of a bunch of sharp lines (dashed lines in Fig. S6*a*), commonly observed in $Al_xGa_{1-x}N$ NWs [15–17] and associated with the localized nature of the electronic states and/or impurity or structural defects.

Fig. S6*b* illustrates the evolution of the CL peaks (obtained after deconvolution into two or three Gaussian components) for $Al_xGa_{1-x}N$-asgr NWs with AlN nominal content ($x > 0$). For GaN-asgr NWs, the value was extracted from the 14 K PL spectrum (Fig. S7). The dependence of the bandgap energy for $Al_xGa_{1-x}N$ alloys (considering no bowing and bowing of 1 eV) is plotted for comparison.

Fig. S6*c* shows the 5 K CL spectra of the $Al_xGa_{1-x}N$-1200 NWs in the spectral range of the NBE emission. The spectra of the $Al_xGa_{1-x}N$-asgr NWs are also included for a better perception of the effects introduced by Eu^{3+}-implantation and RTA in the $Al_xGa_{1-x}N$ NWs. The emission is strongly reduced, indicating that Eu^{3+} ions are preferentially incorporated in the $Al_xGa_{1-x}N$ top-section and that the annealing does not provide full-recovery of the as-grown optical properties. Moreover, the emission shifts to lower or higher energies (depending on the sample), suggesting that the performed treatments may induce *i*) rearrangement of the crystalline lattice (slight composition fluctuations) and *ii*) tensile stress.

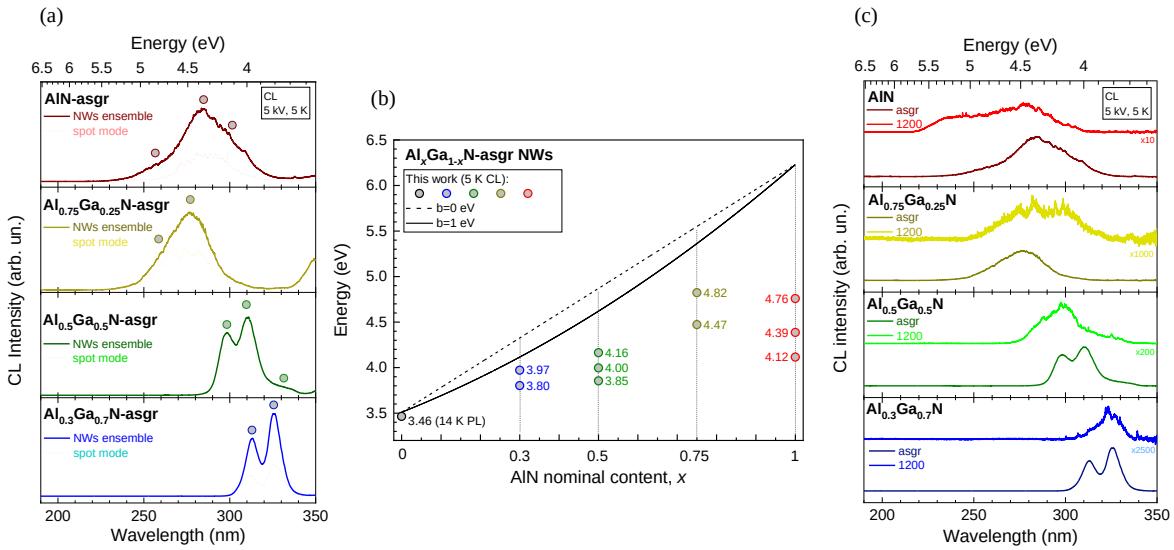

Fig. S6: (*a*) 5 K CL spectra of the $Al_xGa_{1-x}N$-asgr ($x > 0$) obtained for the NW ensemble and single NW (dashed lines). (*b*) CL peaks (circles) versus AlN nominal content. The bandgap evolution $Al_xGa_{1-x}N$ alloys with $b = 0$ eV (dashed line) and $b = 1$ eV (solid line) is plotted for comparison. (*c*) Comparison between the 5 K CL spectra of the $Al_xGa_{1-x}N$-asgr, and $Al_xGa_{1-x}N$-1200 NW ensemble around the NBE emission.

S3.2. PL response of the $Al_xGa_{1-x}N$ NWs

14 K PL spectra of the GaN-asgr (dashed line) and GaN-1000 (solid line) NW ensemble are shown in Fig. S7. For the as-grown NWs, a well-defined near band edge (NBE) emission is observed at 358 nm (~3.46 eV) as well as a low-intensity tail at lower energies, attributed to donor-acceptor pair (DAP) transitions. It is worth mentioning that broad bands related to deep level defects are not observed, indicating a high optical quality of the GaN NWs. After Eu^{3+}-implantation, the crystalline structure is damaged and the NBE is not detected, even after RTA at 1000 ℃. However, the optical activation of the Eu^{3+} ions is achieved with the $^5D_0 \rightarrow {}^7F_2$ transition being the most intense. Overlapped with the Eu^{3+}-related emission, a low-intensity host defect-related broad and asymmetric band is observed in the yellow spectral region. According to previous reports, both implantation and post-implantation thermal annealing were found to induce/promote the formation of optically active defects that contribute to a broad emission band in GaN structures [18,19]. Several hypotheses have been proposed and discussed in the literature about the nature of this band [20–22].

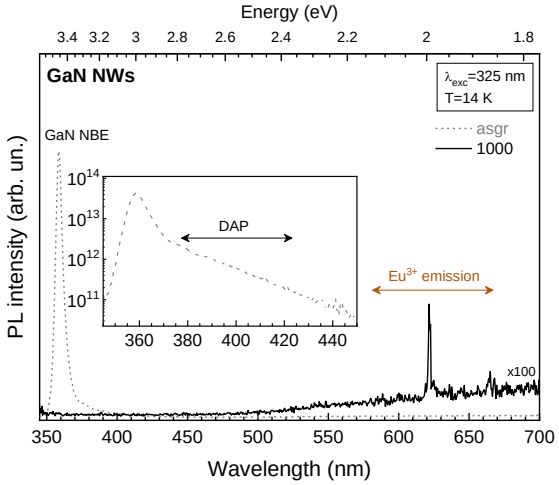

Fig. S7: 14 K PL spectra of the GaN-asgr, and GaN-1000 NW ensemble using laser excitation of 325 nm. Inset corresponds to magnification around the DAP region (in logarithmic scale).

Fig. S8 presents temperature-dependent PL spectra (from 14 K to 300 K) for the $Al_xGa_{1-x}N$-1000 and $Al_xGa_{1-x}N$-1200 NW ensemble using the 325 nm laser excitation: (*a*) $x = 0$; (*b*) $x = 0.3$; (*c*) $x = 0.5$; (*d*) $x = 0.75$; and (*e*) $x = 1$.

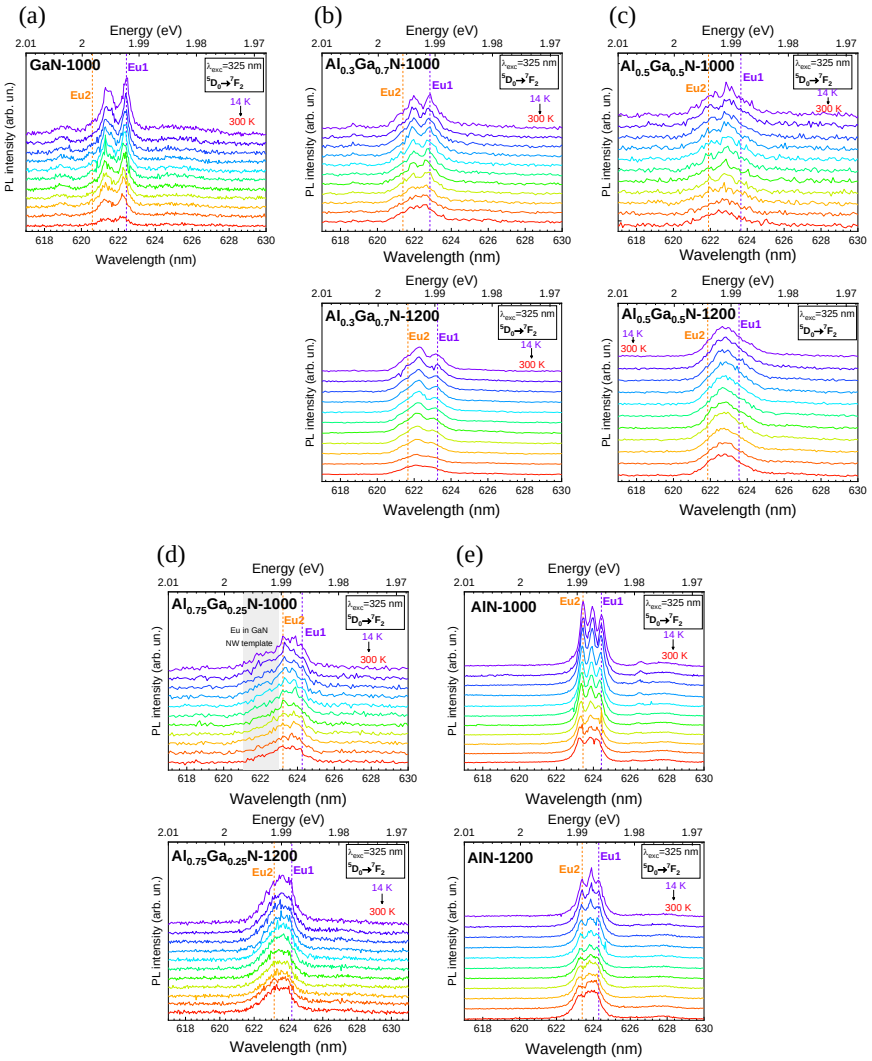

Fig. S8: Temperature-dependent PL spectra around the $^5D_0 \rightarrow {}^7F_2$ transition for $Al_xGa_{1-x}N$-1000, and $Al_xGa_{1-x}N$-1200 NW ensemble: (*a*) $x = 0$; (*b*) $x = 0.3$; (*c*) $x = 0.5$; (*d*) $x = 0.75$; and (*e*) $x = 1$. Vertical dashed lines indicate Eu1 (violet) and Eu2 (orange) centers.

S3.3. Heterogeneity of the $Al_xGa_{1-x}N$ NWs and its impact on the Eu^{3+} emission

Fig. S9*a* shows side-view and top-view SEM images of the $Al_{0.75}Ga_{0.25}$-asgr NWs at different positions of the wafer (20 mm, 15 mm, and 10 mm from the wafer's center). The density of NWs, which is a crucial parameter to the Eu^{3+}-implantation shadowing effects, increases from the wafer's center to the edge. This means that closer to the wafer's center, shadowing effects are less and the implantation may reach the GaN NW template. This effect is represented in the scheme of Fig. S9*b*.

Fig. S9*c* depicts the normalized 14 K HR PL spectra (around the $^5D_0 \rightarrow {}^7F_2$ transition) taken at each position indicated in the SEM images. At 10 mm from the wafer's center, it is possible to detect a significant contribution at higher energies related to Eu^{3+} ions optically active from the GaN NW template. This contribution is not important at 15 and 20 mm from the wafer's center, revealing the impact of the shadowing effect in the depth distribution of Eu^{3+} ions.

Fig. S9*d* shows the integrated PL intensity ratio of the $^5D_0 \rightarrow {}^7F_2$ transition obtained at 300 K and 14 K, $I_{300\ K}/I_{14\ K}$, measured at the different positions of the wafer. For 10 mm, the luminescence shows a higher thermal quenching, which may be related to Eu^{3+} ions that are optically active in the GaN NW template since the quenching is expected to be higher in these hosts, according to Fig. 7*c* (main manuscript).

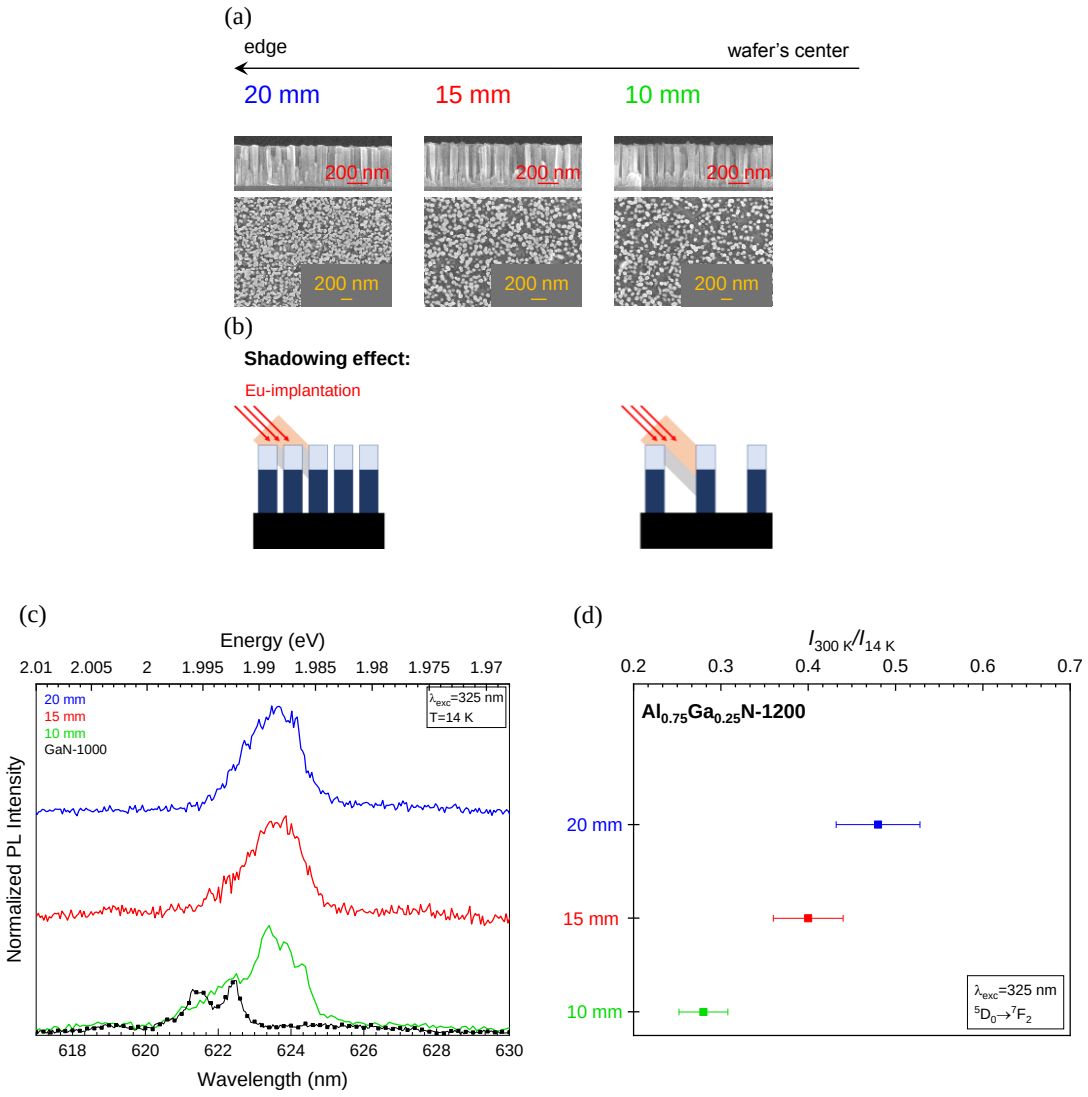

Fig. S9: (*a*) SEM images of the $Al_{0.75}Ga_{0.25}$-asgr NWs in side-view and top-view at different wafer's positions: 20 mm, 15 mm, and 10 mm from the wafer's center. (*b*) Schematic representation of the shadowing effect in samples with different density of NWs. (*c*) 14 K HR PL spectra of the $Al_{0.75}Ga_{0.25}$-asgr NWs under 325 nm laser excitation at the three positions indicated in (a). The 14 K PL spectrum of the GaN-1000 NW ensemble is included for comparison. (*d*) Corresponding $I_{300\ K}/I_{14\ K}$ at the different positions on the wafer.

REFERENCES

[1] V.Y. Davydov, Y.E. Kitaev, I.N. Goncharuk, A.N. Smirnov, J. Graul, O. Semchinova, D. Uffmann, M.B. Smirnov, A.P. Mirgorodsky, R.A. Evarestov, Phonon dispersion and Raman scattering in hexagonal GaN and AlN, Phys. Rev. B. 58 (1998) 12899–12907. https://doi.org/10.1103/PhysRevB.58.12899.

[2] P. Borowicz, M. Latek, W. Rzodkiewicz, A. Łaszcz, A. Czerwinski, J. Ratajczak, Deep-ultraviolet Raman investigation of silicon oxide: Thin film on silicon substrate versus bulk material, Adv. Nat. Sci. Nanosci. Nanotechnol. 3 (2012). https://doi.org/10.1088/2043-6262/3/4/045003.

[3] J. Cardoso, N. Ben Sedrine, A. Alves, M.A. Martins, M. Belloeil, B. Daudin, D.N. Faye, E. Alves, K. Lorenz, A.J. Neves, M.R. Correia, T. Monteiro, Multiple optical centers in Eu-implanted AlN nanowires for solid-state lighting applications, Appl. Phys. Lett. 113 (2018) 201905. https://doi.org/10.1063/1.5048772.

[4] K. Lorenz, E. Nogales, S.M.C. Miranda, N. Franco, B. Méndez, E. Alves, G. Tourbot, B. Daudin, Enhanced red emission from praseodymium-doped GaN nanowires by defect engineering, Acta Mater. 61 (2013) 3278–3284. https://doi.org/10.1016/j.actamat.2013.02.016.

[5] M.W. Ullah, A. Kuronen, A. Stukowski, F. Djurabekova, K. Nordlund, Atomistic simulation of Er irradiation induced defects in GaN nanowires, J. Appl. Phys. 116 (2014) 124313. https://doi.org/10.1063/1.4896787.

[6] D.N. Faye, X. Biquard, E. Nogales, M. Felizardo, M. Peres, A. Redondo-Cubero, T. Auzelle, B. Daudin, L.H.G. Tizei, M. Kociak, P. Ruterana, W. Möller, B. Méndez, E. Alves, K. Lorenz, Incorporation of Europium into GaN Nanowires by Ion Implantation, J. Phys. Chem. C. 123 (2019) 11874–11887. https://doi.org/10.1021/acs.jpcc.8b12014.

[7] J.M. Wagner, F. Bechstedt, Phonon deformation potentials of α-GaN and -AlN: An ab initio calculation, Appl. Phys. Lett. 77 (2000) 346–348. https://doi.org/10.1063/1.127009.

[8] J.B. Gruber, U. Vetter, T. Taniguchi, G.W. Burdick, H. Hofsäss, S. Chandra, D.K. Sardar, Spectroscopic analysis of Eu^{3+} in single-crystal hexagonal phase AlN, J. Appl. Phys. 110 (2011) 023104. https://doi.org/10.1063/1.3609076.

[9] T. Andreev, N.Q. Liem, Y. Hori, M. Tanaka, O. Oda, D.L.S. Dang, B. Daudin, Optical transitions in Eu^{3+} ions in GaN:Eu grown by molecular beam epitaxy, Phys. Rev. B - Condens. Matter Mater. Phys. 73 (2006) 3–8. https://doi.org/10.1103/PhysRevB.73.195203.

[10] K. Binnemans, Interpretation of europium(III) spectra, Coord. Chem. Rev. 295 (2015) 1–45. https://doi.org/10.1016/j.ccr.2015.02.015.

[11] H. Morkoç, Nitride Semiconductor Devices : Principles and Simulation Properties of Group-IV , III-V and II-VI Semiconductors Nitride Semiconductors, 2008.

[12] I. Vurgaftman, J.R. Meyer, L.R. Ram-Mohan, Band parameters for III-V compound semiconductors and their alloys, J. Appl. Phys. 89 (2001) 5815–5875. https://doi.org/10.1063/1.1368156.

[13] T. Koppe, H. Hofsäss, U. Vetter, Overview of band-edge and defect related luminescence in aluminum nitride, J. Lumin. 178 (2016) 267–281. https://doi.org/10.1016/j.jlumin.2016.05.055.

[14] A.M. Siladie, G. Jacopin, A. Cros, N. Garro, E. Robin, D. Caliste, P. Pochet, F. Donatini, J. Pernot, B. Daudin, Mg and in Codoped p-type AlN Nanowires for pn Junction Realization, Nano Lett. 19 (2019) 8357–8364. https://doi.org/10.1021/acs.nanolett.9b01394.

[15] A. Pierret, C. Bougerol, M. den Hertog, B. Gayral, M. Kociak, H. Renevier, B. Daudin, Structural and optical properties of $Al_xGa_{1-x}N$ nanowires, Phys. Status Solidi - Rapid Res. Lett. 7 (2013) 868–873. https://doi.org/10.1002/pssr.201308009.
[16] A. Pierret, C. Bougerol, S. Murcia-Mascaros, A. Cros, H. Renevier, B. Gayral, B. Daudin, Growth, structural and optical properties of AlGaN nanowires in the whole composition range, Nanotechnology. 24 (2013) 115704. https://doi.org/10.1088/0957-4484/24/11/115704.
[17] M. Belloeil, B. Gayral, B. Daudin, Quantum Dot-Like Behavior of Compositional Fluctuations in AlGaN Nanowires, Nano Lett. 16 (2016) 960–966. https://doi.org/10.1021/acs.nanolett.5b03904.
[18] J. Rodrigues, S.M.C. Miranda, A.J.S. Fernandes, E. Nogales, L.C. Alves, E. Alves, G. Tourbot, T. Auzelle, B. Daudin, B. Méndez, T. Trindade, K. Lorenz, F.M. Costa, T. Monteiro, Towards the understanding of the intentionally induced yellow luminescence in GaN nanowires, Phys. Status Solidi Curr. Top. Solid State Phys. 10 (2013) 667–672. https://doi.org/10.1002/pssc.201200714.
[19] N. Ben Sedrine, T.C. Esteves, J. Rodrigues, L. Rino, M.R. Correia, M.C. Sequeira, A.J. Neves, E. Alves, M. Bockowski, P.R. Edwards, K.P. O'Donnell, K. Lorenz, T. Monteiro, Photoluminescence studies of a perceived white light emission from a monolithic InGaN/GaN quantum well structure, Sci. Rep. 5 (2015) 3–9. https://doi.org/10.1038/srep13739.
[20] M.A. Reshchikov, H. Morkoç, Luminescence properties of defects in GaN, J. Appl. Phys. 97 (2005) 1–95. https://doi.org/10.1063/1.1868059.
[21] M.A. Reshchikov, M. Vorobiov, D.O. Demchenko, Ozgur, H. Morkoç, A. Lesnik, M.P. Hoffmann, F. Hörich, A. Dadgar, A. Strittmatter, Two charge states of the C_N acceptor in GaN: Evidence from photoluminescence, Phys. Rev. B. 98 (2018) 125207. https://doi.org/10.1103/PhysRevB.98.125207.
[22] M.A. Reshchikov, J.D. McNamara, H. Helava, A. Usikov, Y. Makarov, Two yellow luminescence bands in undoped GaN, Sci. Rep. 8 (2018) 1–11. https://doi.org/10.1038/s41598-018-26354-z.
[23] K. Wang, K.P. O'Donnell, B. Hourahine, R.W. Martin, I.M. Watson, K. Lorenz, E. Alves, Luminescence of Eu ions in $Al_xGa_{1-x}N$ across the entire alloy composition range, Phys. Rev. B. 80 (2009) 125206. https://doi.org/10.1103/PhysRevB.80.125206.